Tectonophysics 868 (2023) 230112

Contents lists available at ScienceDirect

Tectonophysics

journal homepage: www.elsevier.com/locate/tecto

Anisotropic structure of the normally-dipping and flat slab segments of the Alaska subduction zone: Insights from receiver function analysis

Anne A. Haws *, Maureen D. Long, Yantao Luo

Department of Earth and Planetary Sciences, Yale University, PO Box 208109, New Haven, CT 06520, USA

ARTICLE INFO

Keywords:
Subduction
Seismic anisotropy
Alaska
Yakutat
Flat slab
Receiver functions

ABSTRACT

The complex tectonic setting of south-central Alaska is characterized by a transition from normally-dipping subduction of the Pacific plate in the west to near-flat slab subduction of the overthickened Yakutat microplate in the east. Many previous studies have characterized both the isotropic and anisotropic subsurface structure of this region, but only a few studies have characterized anisotropy using receiver functions. Here, we present anisotropy-aware receiver function analysis for two transects of permanent seismic stations in south-central Alaska, one covering a normally-dipping segment of the subduction zone, and one covering the adjacent flat slab segment. Beneath the normally-dipping segment, there is evidence for shearing and possibly serpentinization at the top of the slab in the shallow forearc, and for variation in mantle flow geometry with depth, possibly a result of oblique subduction and/or the adjacent flat slab segment, or an arc magmatism-related process. Additionally, there appears to be significant crustal deformation associated with the volcanic arc. We also identify significant crustal deformation and anisotropy along the flat slab segment, likely a result of the subducting Yakutat microplate, with crustal deformation geometry appearing to vary along the transect. There also appears to be evidence for water-rich conditions at the top of the flat slab, shedding light on the distribution of volatiles in a flat slab setting that lacks an active volcanic arc.

1. Introduction

South-central Alaska (Fig. 1) is an active and complex convergent margin setting, with terrane accretion, flat slab subduction, and normally-dipping subduction all occurring along the southern coast (Eberhart-Phillips et al., 2006). From the western half of the Kenai Peninsula out to the Aleutians, the Pacific plate subducts beneath the North American plate, dipping at a fairly typical angle (~30–40°; Gou et al., 2019). From the eastern side of the Kenai Peninsula to the Queen Charlotte/Fairweather transform system in eastern Alaska, however, the Yakutat microplate is accreting to, and subducting beneath, the North American continent (Plafker and Berg, 1994; Eberhart-Phillips et al., 2006; Fuis et al., 2008). These radically different subduction geometries manifest at the surface, with the normally-dipping Pacific slab associated with a typical subduction zone volcanic arc, while the nearly flat Yakutat slab is associated with a gap in volcanism in central Alaska and significant deformation and uplift of the overriding plate (Plafker and Berg, 1994; Eberhart-Phillips et al., 2006). Southern Alaska thus affords an opportunity to study substantially different slab geometries in adjacent slab segments, similar to work that has been done on the Peru and Pampean flat slab segments in South America (e.g., Gilbert et al., 2006; Wagner et al., 2006; Bishop et al., 2017; Kumar et al., 2016).

The subducting Yakutat microplate, whose inferred extent offshore and beneath south-central Alaska is shown in Fig. 1, results in very shallowly dipping subduction (for simplicity, we refer to this region as a "flat slab" segment, even though strictly speaking it is shallowly dipping rather than truly flat). The Yakutat terrane is inferred to be an oceanic plateau (e.g., Christeson et al., 2010; Worthington et al., 2012) with crustal thickness ~15–30 km (Eberhart-Phillips et al., 2006; Rondenay et al., 2008; Worthington et al., 2012; Kim et al., 2014). This is more than double that of typical Pacific plate crust, which Kim et al. (2014) have estimated to be ~6–8 km beneath southern Alaska. The dip of the flat slab is <5° near the coast and steepens to ~20–25° farther inland (Kim et al., 2014; Ferris et al., 2003). Previous studies have examined the subsurface characteristics of south-central Alaska, including the extent (Eberhart-Phillips et al., 2006; Fuis et al., 2008) and thickness (Ferris et al., 2003; Rossi et al., 2006; Rondenay et al., 2008; Kim et al., 2014) of the subducting Yakutat crust and slab, seismic velocity

* Corresponding author.
E-mail address: anne.haws@yale.edu (A.A. Haws).

https://doi.org/10.1016/j.tecto.2023.230112
Received 18 April 2023; Received in revised form 16 September 2023; Accepted 27 September 2023
Available online 4 November 2023

heterogeneity via seismic tomography (e.g., Eberhart-Phillips et al., 2006; Tian and Zhao, 2012; Wang and Tape, 2014; Martin-Short et al., 2016, 2018; Gou et al., 2019), crustal deformation patterns (Schulte--Pelkum et al., 2020), and subsurface features that may be associated with sediments (Kim et al., 2014), melt (Rondenay et al., 2010), or slab dehydration (Rondenay et al., 2008).

The anisotropic structure of Alaska has also been investigated in considerable detail in past studies. Seismic anisotropy observations are a powerful tool for understanding deformation and other processes at depth. Mantle deformation and flow may lead to the formation of aligned olivine fabrics (lattice preferred orientation or LPO), which exhibit a bulk seismic anisotropy (Karato et al., 2008) in mantle rocks. Anisotropy may also arise from the deformation-induced alignment of other minerals as well, including those in crustal rocks (e.g., Brownlee et al., 2017) and hydrous mantle phases such as serpentine (e.g., Mainprice and Ildefonse, 2009); both crustal deformation and the distribution of hydrous minerals are of particular interest in subduction zones. Several previous studies have addressed anisotropy in south-central Alaska using a variety of methods, including SKS splitting (e.g., Hanna and Long, 2012; Perttu et al., 2014; Venereau et al., 2019; McPherson et al., 2020), shear wave splitting from local earthquake sources (Karlowska et al., 2021; Richards et al., 2021), surface wave tomography (Wang and Tape, 2014), body wave tomography (Tian and Zhao, 2012; Gou et al., 2019), and P-to-S receiver functions (RFs) (Schulte-Pelkum et al., 2020).

In general, SKS splitting studies indicate subduction-parallel fast splitting directions in the forearc region where the normally-dipping Pacific plate is subducting beneath the southwestern Kenai peninsula (Hanna and Long, 2012; Perttu et al., 2014; Venereau et al., 2019; McPherson et al., 2020), with a transition to trench-parallel fast splitting directions beneath the arc (Venereau et al., 2019; McPherson et al., 2020). The SKS fast splitting directions associated with Yakutat slab subduction generally follow a similar pattern (Hanna and Long, 2012; Perttu et al., 2014; Venereau et al., 2019; McPherson et al., 2020). McPherson et al. (2020) suggest that the change in fast splitting direction results from SKS phases sampling more of the mantle wedge in the backarc than the forearc. The fast directions suggested by the anisotropic tomography studies of Tian and Zhao (2012) and Gou et al. (2019) appear to corroborate these observations over some depth ranges, although there is also evidence for changing anisotropic orientations and intensities with depth. Results from local shear wave splitting studies, which rule out significant contributions to observed anisotropy from the slab lithospheric mantle and the subslab mantle, indicate fast directions changing from arc-parallel in the forearc to arc-perpendicular in the backarc (Karlowska et al., 2021; Richards et al., 2021), although Richards et al. (2021) note that their results appear to agree with SKS splitting results in the most trenchward regions of the forearc. Karlowska et al. (2021) suggest that the lack of correlation between local shear wave and SKS splitting results could indicate that the latter may be primarily controlled by intra- and sub-slab anisotropy, and are thus less sensitive to anisotropy in the mantle wedge. Additionally, Karlowska et al. (2021) suggest the presence of a serpentinized layer at the top of the Pacific slab based on their observations.

Although shear wave splitting can place important constraints on the dominant anisotropic orientation beneath a given station, it is not generally possible to identify the specific layers in which this anisotropy originates. Additionally, because shear wave splitting measurements are path-integrated, it is also challenging to resolve variations in anisotropic orientation with depth. Receiver functions are a particularly powerful tool for understanding the details of layered anisotropic structure beneath a seismic station. RFs are sensitive to sharp seismic discontinuities and can thus be used to characterize specific interfaces, including contrasts in anisotropy (e.g., Levin and Park, 1997; Ford et al., 2016). They are therefore complementary to shear wave splitting and anisotropic tomography studies, which cannot resolve such boundaries. Schulte-Pelkum et al. (2020) used anisotropy-aware P-to-S receiver functions to better constrain anisotropic layering and crustal deformation in south-central Alaska. This technique, however, has not been

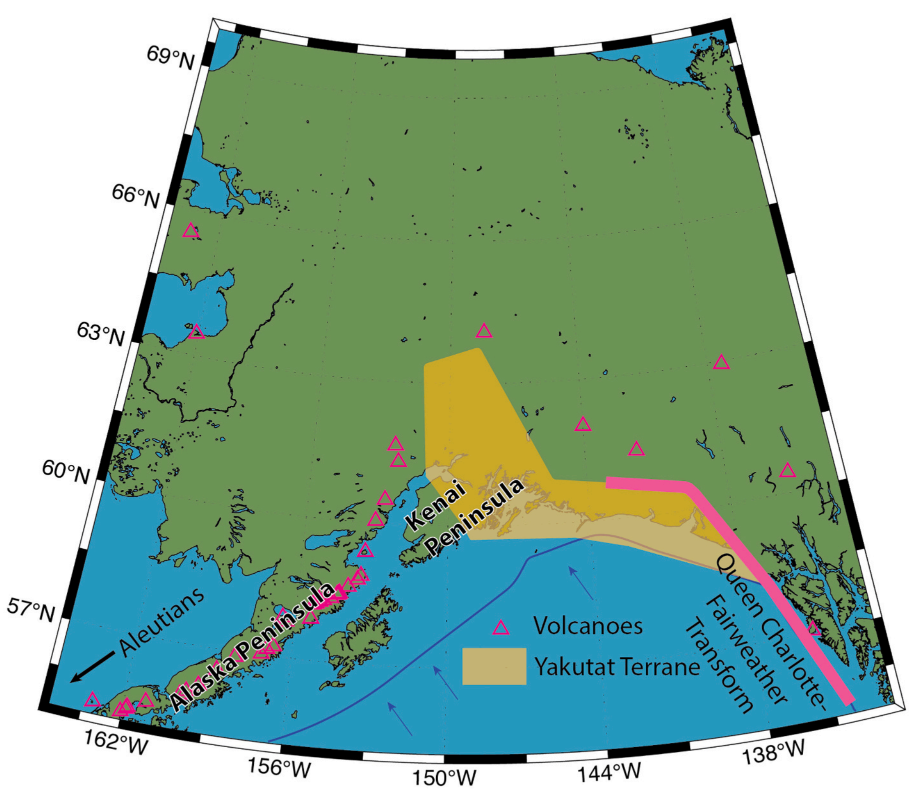

Fig. 1. Map of Alaska showing the extent of the Yakutat terrane (orange patch) and locations of volcanoes (after Miller et al., 2018, Fuis et al., 2008, and Plafker and Berg, 1994; volcano locations from the Smithsonian Global Volcanism Program).

widely applied to mantle wedge and subducting slab structures in south-central Alaska.

In this study we focus on anisotropy-aware RF analysis, with the goal of better constraining anisotropic layering in the mantle wedge and subducting slab beneath south-central Alaska. We aim to identify specific anisotropic features that can be linked to subduction zone processes; for example, anisotropy-aware receiver function studies in other subduction zones have led to the identification of hydrous phases in the mantle wedge (e.g., Park et al., 2004; Nikulin et al., 2009, 2019; McCormack et al., 2013; Krueger and Wirth, 2017), and have been used to examine layered anisotropy in flat slab settings (e.g., Bar et al., 2019; Nikulin et al., 2019).

Here we present a detailed examination of directionally-dependent RF traces at a small set of carefully selected stations in south-central Alaska. We selected four stations along a convergence-parallel transect above a normally-dipping subduction segment, and four stations along a transect above an adjacent flat-dipping segment. Our study has several specific goals. First, we aim to examine the first-order structure of the adjacent subduction segments (e.g., overriding crust thickness, depth to slab Moho and slab top) in detail, using directionally-dependent analysis to understand the possible role of lateral heterogeneity in interpreting these structures. Second, we aim to characterize in detail the layered anisotropy beneath each station, including anisotropy within the overriding plate crust, the mantle wedge, and the shallow portions of the slab itself. We are particularly interested in identifying interfaces within or between these layers that show evidence of seismic anisotropy, and interpreting these anisotropy indicators in terms of deformation and/or the presence of hydrous (and therefore strongly anisotropic) minerals such as serpentine. Characterizing the geometry and lateral continuity of anisotropic layers along each of our transects can shed light on the length scales of coherent crustal and mantle deformation and potentially on the lateral extent of structures such as partial melt lenses and serpentinized regions of the mantle wedge. Third, we aim to compare our results from the normally-dipping and flat-slab segments to understand the role that the subducting Yakutat microplate plays in overriding plate deformation, volatile cycling, and slab morphology.

2. Methods & data

2.1. Receiver functions and harmonic decomposition

P-to-S receiver functions are time series computed from three-component seismograms that image the velocity structure beneath the station. When a P-wave encounters a flat-lying, isotropic contrast in impedance (the product of seismic velocity and density), it is partially converted to an SV wave, with the amplitude of the Ps wave depending on the incidence angle and the impedance contrast. This SV wave arrives after the direct P wave at a delay time that reflects the velocity structure as well as the depth of the interface beneath the receiver; i.e., SV waves converted at shallower interfaces will arrive earlier than SV waves converted at deeper ones. Both the direct P arrival and the SV arrival can be observed on radial component receiver functions. A positive arrival on the radial component (that is, an arrival with the same polarity as the direct P arrival) is associated with a velocity increase with depth, while a negative arrival is associated with a velocity decrease with depth. (In this paper, we use a plotting convention that assigns a blue color to positive arrivals and a red color to negative ones.)

When a P wave encounters a dipping or anisotropic interface, some energy is also converted to an SH wave, which has a polarization direction that is (nearly) orthogonal to both the original P wave and the converted SV phase; these SH arrivals can be observed on the transverse component receiver functions (Levin and Park, 1997). Therefore, significant energy on the transverse receiver function component may be indicative of dipping and/or anisotropic interfaces beneath the receiver. Polarity changes of transverse component arrivals with backazimuth are related to the structure of the anisotropic and/or dipping interface. Dipping, isotropic interfaces produce a "two-lobed" signal on the transverse component, whose polarity flips in 180° backazimuthal intervals (Levin and Park, 1997; Ford et al., 2016). This is also the case for anisotropic interfaces with a dipping symmetry axis. For an anisotropic interface with a horizontal axis of symmetry, a "four-lobed" pattern is observed; in this case, the polarity of the arrival on the transverse component flips in 90° backazimuthal intervals (Levin and Park, 1997; Ford et al., 2016). The presence of dipping and/or anisotropic interfaces also affects the amplitude and timing of arrivals on the radial component (e.g., Levin and Park, 1997; Schulte-Pelkum and Mahan, 2014a, 2014b).

Identifying and characterizing dipping and/or anisotropic structures from visual inspection alone is typically difficult in cases where structures are complex. Therefore, in our study we also implement a harmonic decomposition approach to modeling RFs (e.g., Bianchi et al., 2010; Olugboji and Park, 2016; Park and Levin, 2016; Ford et al., 2016) to elucidate the nature of interfaces at depth and quantify their characteristics. This method takes advantage of the predictions for the harmonic behavior of both radial and transverse component RF traces for isotropic, dipping, and/or anisotropic interfaces (e.g., Schulte-Pelkum and Mahan, 2014a, 2014b; Olugboji and Park, 2016). Specifically, it models the harmonic behavior of RF traces as a function of backazimuth with five components (where k is the harmonic order and θ is the backazimuth): a $k = 0$ constant term that accounts for isotropic velocity contrasts or vertical anisotropic symmetry axes (i.e., signals that are constant across backazimuths); two $k = 1$ terms, whose signals display $\sin(\theta)$ or $\cos(\theta)$ periodicity with backazimuth and are associated with dipping interfaces and/or dipping anisotropic symmetry axes; and two $k = 2$ terms, whose signals display $\sin(2\theta)$ or $\cos(2\theta)$ periodicity with backazimuth and are associated with horizontal anisotropic symmetry axes. Signals on the $\cos(\theta)$ and $\sin(\theta)$ terms indicate primarily north-south and east-west oriented axes of symmetry or dip directions, respectively; signals on the $\cos(2\theta)$ terms are associated with N-S or *E*-W oriented horizontal anisotropy, while signals on the $\sin(2\theta)$ terms are associated with NW-SE or NE-SW oriented horizontal anisotropy (e.g., Bianchi et al., 2010; Park and Levin, 2016; Ford et al., 2016; Bar et al., 2019). This harmonic decomposition modeling can thus be used to more easily identify anisotropic and/or dipping interfaces, and to approximate their orientations (see Fig. 3 for a summary of interpretations for these signals). In addition, the harmonic decomposition also produces unmodelled harmonic terms, reflecting more complex structures that cannot be explained by dipping and/or anisotropic interfaces (Park and Levin, 2016). Therefore, if the amplitudes of the unmodeled terms are high relative to the modeled terms, the complex structure beneath the receiver is likely not well-approximated by dipping and/or anisotropic interfaces alone and should be interpreted with caution.

The relative amplitudes of the $k = 1$ terms can be used to estimate the direction of the tilt axis for anisotropy with a plunging symmetry axis, or the downdip direction for a dipping isotropic interface (Olugboji and Park, 2016; Bar et al., 2019). This is calculated using Eq. (3) of Olugboji and Park (2016),

$$\zeta = tan^{-1}(\mathrm{RF}_{\cos\theta}/\mathrm{RF}_{\sin\theta}) \tag{1}$$

where ζ is the tilt direction, and $\mathrm{RF}_{\cos\theta}$ and $\mathrm{RF}_{\sin\theta}$ are the amplitudes of the $k = 1$ components of the harmonic decomposition gather at the delay time of interest. For dipping interfaces, the tilt direction is also influenced by the sign of the constant term, so calculated tilt directions for $k = 1$ signals associated with strong negative velocity gradients are rotated by 180°. It is also important to note that these directions have a 180° ambiguity for a plunging symmetry axis. When applied to an anisotropic interface, this calculation provides the tilt direction for a fast axis of symmetry, but a slow axis of symmetry oriented 180° from the calculated fast axis would also be consistent with the harmonic decomposition results (Olugboji and Park, 2016; Bar et al., 2019). An additional 180° ambiguity is introduced in situations in which it is unknown whether the interface of interest is associated with the top or the

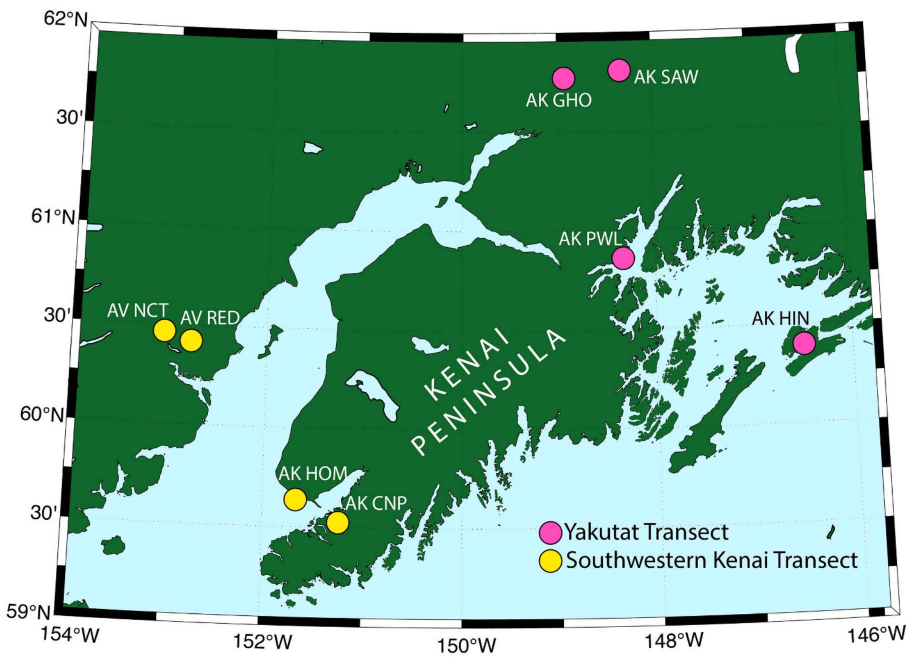

Fig. 2. Map of the study area showing the stations selected for the Yakutat Transect (pink) and Kenai Transect (yellow). (For interpretation of the references to color in this figure legend, the reader is referred to the web version of this article.)

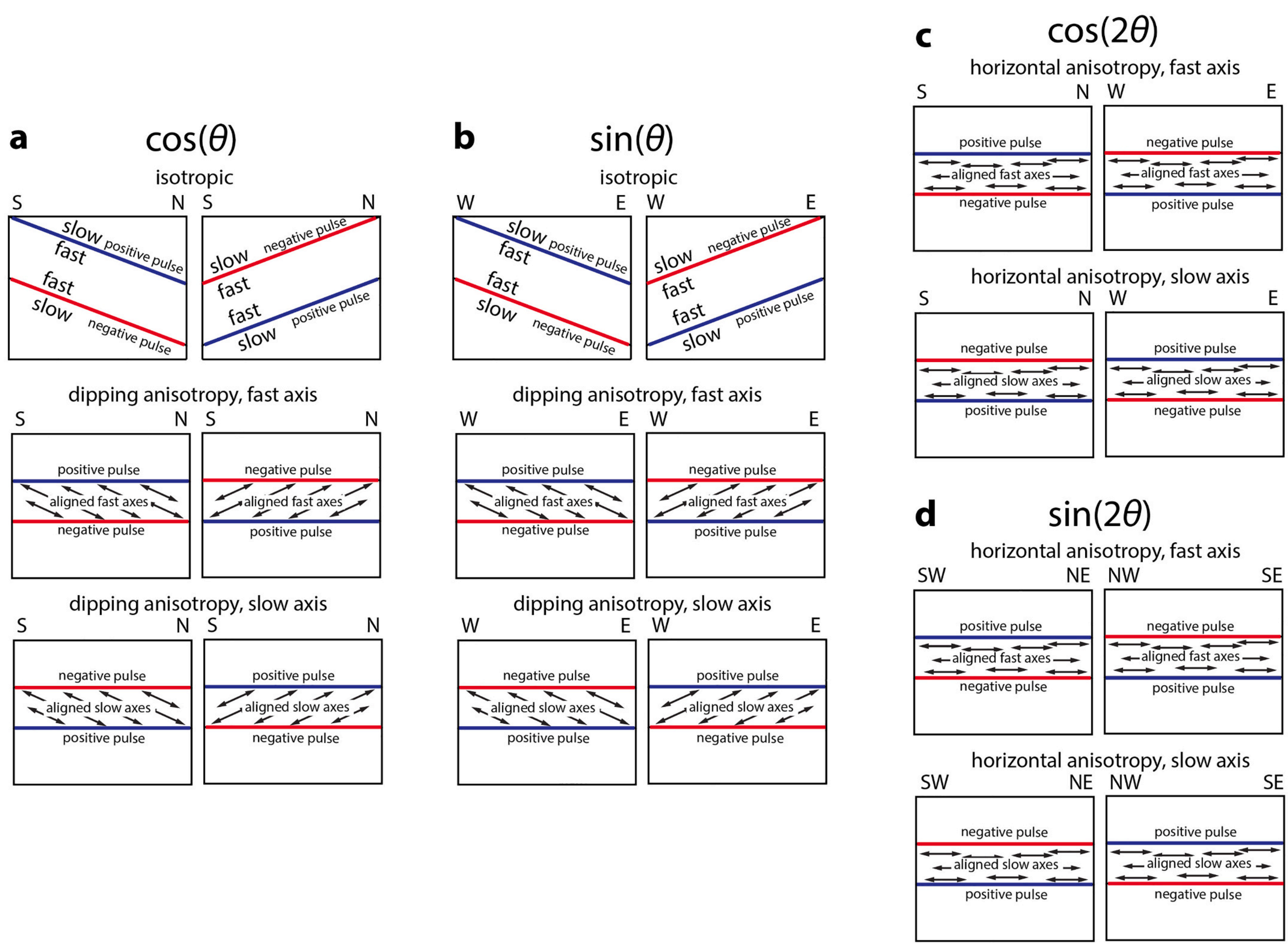

Fig. 3. Sketches showing the expected signal polarity for various dipping or anisotropic interfaces for the four non-constant components of the harmonic decomposition gather: cos(θ) (a); sin(θ) (b); cos(2θ) (c); and sin(2θ) (d).

bottom of an anisotropic layer. Therefore, for each tilt axis, two values are estimated: the first is the tilt direction assuming a fast axis associated with the top interface of an anisotropic layer or a slow axis associated with the bottom interface, and the second is the corresponding direction assuming a slow axis associated with a top interface, or a fast axis associated with a bottom interface. A final caveat associated with these tilt axes is that while they are reported herein to the degree, it is important to note that these are only estimates to be interpreted generally, as the exact value reported is sensitive to parameters such as cutoff frequency and may be impacted by signals from neighboring interfaces. They are therefore used to constrain the approximate tilt direction of anisotropy for more general interpretations, rather than interpreted as exact orientations.

2.2. Data acquisition and processing

We selected 8 stations in south-central Alaska with long data records and high data quality, which make up two approximately convergence-parallel transects, as shown in Fig. 2. The first transect overlies a normally-dipping segment of the Pacific slab and extends across the forearc; it begins on the southwestern tip of the Kenai Peninsula and extends northwest (herein referred to as the "Kenai transect"). Two of the stations (AK HOM and AK CNP) are located in the forearc, and AV NCT and AV RED are located on or near the arc. The second transect (herein the "Yakutat transect") overlies the subduction of the Yakutat microplate. These stations are, by increasing distance from the trench, AK HIN, AK PWL, AK SAW, and AK GHO. These stations cover what would be the forearc region of the flat slab segment, although this part of the subduction zone lacks an active volcanic arc. The relative proximity of SAW and GHO allows for the examination of local heterogeneities in the complex flat slab setting.

Broadband waveform data was accessed from the IRIS (Incorporated Research Institutions for Seismology) DMC (Data Management Center) using Pyweed. We selected teleseismic events with moment magnitudes >6.0 and epicentral distances between 30 and 100° from the study area. A map of earthquakes used in our analysis is shown in Fig. 4. We used events recorded between the installation date of each station and the end of 2020. Start dates vary by station, but we have a minimum five years of data at all stations. 648 individual events were included in this study, and many were recorded by multiple stations in our transects. We rotated horizonal component data into the radial (R) and transverse (T) orientations and bandpass filtered from 0.2 to 2 Hz using the Seismic Analysis Code (SAC). Data were then visually inspected using the Program for Array Seismic Studies of the Continental Lithosphere (PASSCAL) Quick Look (PQL) software. We selected records with clear P-wave arrivals on the vertical (Z) component and high signal-to-noise ratios on the R and T components for RF analysis. Before calculating RFs, P-wave arrivals were picked manually using SAC to set the time window for the cross-correlation. We calculated RFs using the multiple-taper cross-correlation technique of Park and Levin (2000) with a 1 Hz low-pass cutoff, and then binned and stacked them by backazimuth. Following Ford et al. (2016) and Bar et al. (2019), harmonic decomposition models were calculated for target depths between 20 and 100 km at intervals of 10 km. Traces were migrated to the target depth by assuming a Ps conversion occurs at the depth of interest and using a velocity model to calculate the associated delay time, which is then set to 0 s, following conventions used by previous studies. The ak_135 velocity model of Kennett et al. (1995) was used for the Kenai stations, and the local velocity model of Daly et al. (2021) was used for the Yakutat stations. Tilt directions were calculated for interfaces of interest as described in

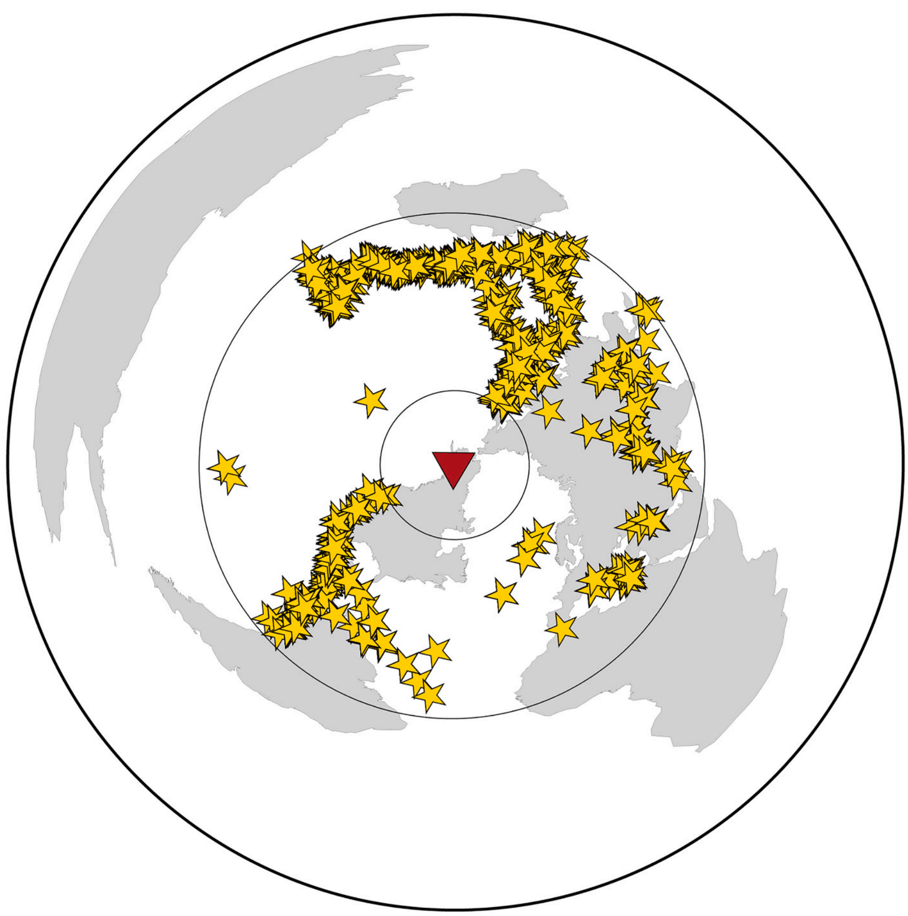

Fig. 4. Map showing locations of all events used in this study (stars). The study area is indicated by the inverted triangle.

section 2.1.

Receiver functions were also binned and stacked by epicentral distance (Figs. S1-S8) to confirm that the arrivals we interpret are associated with primary conversions and not multiply scattered phases. Because multiples cannot be distinguished from primary conversions based on backazimuthal gathers alone, care must be taken to ensure that they are not mistakenly interpreted as such. This can be addressed by examining the epicentral distance gathers. Multiples are characterized by strong moveout in which delay time increases with increasing epicentral distance (e.g., Olugboji and Park, 2016). To demonstrate that our interpreted signals do not arise from multiples, we have highlighted each interface we interpret below the depth of the continental Moho on the epicentral distance gathers, and show estimated arrival times of Moho multiples exhibiting this characteristic moveout for comparison (Figs. S1-S8).

3. Station-by-station results

Here we describe in detail the results for each of the eight stations examined in this study. For each station, we show backazimuthal RF gathers with interpreted interfaces marked on both the radial and transverse components, including the likely overriding plate Moho and slab Moho (Figs. 5-12). We also show harmonic decomposition results for each station, with major interfaces marked. For simplicity, we show harmonic decomposition models migrated to a target depth of 20 km in the main manuscript (Figs. 5-12), as this is the approximate depth at which we begin interpreting the RFs. Harmonic decomposition gathers for other target depths of interest at each station are provided in the Supplementary Information (Figs. S9-S16). Some of the features discussed in the text are particularly clear in the depth-specific harmonic decomposition gathers shown in Supplementary Figs. S9-S16. High-amplitude conversions on the backazimuthal and harmonic decomposition gathers were selected for interpretation. As an additional check on the reliability of interpreted interfaces, the amplitude of the arrival on the modeled component of the harmonic decomposition gather was compared to the unmodeled component; interfaces with relatively strong unmodeled components were not interpreted. As a starting point for interpretation, conversions that may correspond to the overriding plate or slab Moho, which are usually associated with a positive velocity contrast with depth, are identified as high-amplitude, positive arrivals on the radial component of the backazimuthal gather and the constant term of the harmonic decomposition gather. As discussed in section 3.2, however, this may not necessarily be the case, so these criteria are used as a starting point, and further interpretations are made based on the context of the other interfaces of interest, results from neighboring stations, and the regional structure. On the backazimuthal gathers, we also mark interfaces that have strong constant terms but likely correspond to features other than the overriding plate and slab Moho; interfaces associated with strong non-constant terms, but little or no energy on the constant terms, are identified on the harmonic decomposition gathers only. Note that each tilt direction was calculated using amplitudes from the harmonic decomposition gather migrated to a target depth of the nearest multiple of ten (e.g., the tilt direction for a ~55 km interface is calculated from the $k = 1$ amplitudes of the harmonic decomposition gather migrated to 60 km), even though we only show 20 km target depth models in the main text.

3.1. Kenai transect

3.1.1. AK CNP

Station CNP, the station nearest to the trench in the Kenai transect, is located ~290 km from the trench; backazimuthal gathers and harmonic decomposition results for this station are shown in Fig. 5. We identify three positive-amplitude pulses on the constant term of the harmonic decomposition gather that could feasibly correspond to the overriding plate and/or slab Moho, located at depths of approximately ~15 km, ~35 km, and ~50 km (Fig. 5a). On the radial component backazimuthal gather, the first of these pulses is strongly visible in the backazimuthal range from ~200–360°, but disappears at other backazimuths. The pulse corresponding to the interface at ~35 km is present across the entire backazimuthal range, as is the ~50 km interface. We interpret the ~35 km interface as most likely corresponding to the Moho of the overriding plate, and the ~50 km interface as most likely corresponding to the subducting slab Moho.

We observe two interfaces within the continental crust that appear to be associated with strong anisotropic and/or dipping signals. Both of these interfaces are associated with isotropic impedance contrasts, and are thus marked on the radial component of the backazimuthal gather as well as the harmonic decomposition gather (Fig. 5). The first of these interfaces is the ~15 km velocity increase discussed above, while the second is a velocity decrease at ~25 km. The ~15 km interface is associated with a significant negative $\sin(\theta)$ pulse, suggesting that this interface is dipping and/or anisotropic. The tilt direction calculated for this interface is 248°/68°. The ~25 km velocity decrease is associated with a large, positive $\sin(\theta)$ pulse (Fig. 3b), and the tilt direction calculated here is 285°/105°. Given the signal polarities for the constant terms and $\sin(\theta)$ terms, these two interfaces may be associated with the top and bottom of a fast layer in the continental crust that is dipping approximately west, but the top and bottom of a west-dipping fast axis of anisotropy or an east-dipping slow axis of anisotropy are also possible interpretations of these signals (see Fig. 3b).

If the slab crust is indeed 6–8 km thick (Kim et al., 2014), the depth of the interpreted slab Moho indicates that the slab top is probably located at ~40–45 km beneath CNP. Thus, interfaces located between the continental Moho at ~35 km and the slab top at ~40–45 km should correspond to mantle wedge structures. Beneath CNP, there is one such interface; it involves a large $\sin(2\theta)$ component and is located at ~45 km (Fig. 5b). This may correspond to a feature at or near the top of the Pacific slab. This interface has little energy on the $k = 0$ or $k = 1$ terms, suggesting that it is primarily associated with horizontally-oriented anisotropy, and because it appears mostly on the $\sin(2\theta)$ component, its fast orientation is approximately NW-SE or NE-SW (depending on whether it is the top or bottom interface of an anisotropic layer, or whether it is associated with a slow or fast axis of symmetry).

We also infer some features within the mantle lithosphere of the slab itself (Fig. 5). These include a pulse visible on the $\sin(\theta)$ term at ~60 km depth whose tilt direction is 101°/281°, approximately east or west, a pulse visible mostly on the $\cos(\theta)$ term at ~80 km depth whose tilt direction is 28°/208°, approximately north or south, and a constant-term velocity decrease at ~85 km that is also associated with energy on the $\sin(2\theta)$ component, implying anisotropy. This velocity decrease could plausibly represent the base of the slab, suggesting a slab lithospheric thickness of ~40 km, and implying a contrast in anisotropy between the slab lithosphere and the asthenospheric mantle beneath.

3.1.2. AK HOM

Station HOM (Fig. 6) is located ~315 km from the trench. Here, we identify a positive pulse on the radial component RFs that likely corresponds to the continental Moho at ~20 km, and another prominent pulse that we attribute to the slab Moho at ~70 km. We note, however, that the pulse associated with the overriding plate Moho is not visible at all backazimuths (Fig. 6a), and while it does appear on the constant term of the harmonic decomposition (Fig. 6b), it appears at the shoulder of the main P arrival pulse. The slab Moho arrival is associated with a large pulse on the $\sin(2\theta)$ component, indicating the presence of anisotropy with either a NE-SW or NW-SE fast orientation. Above the inferred slab Moho at ~65 km, there is a large, negative $\sin(\theta)$ pulse (Fig. 6b), which may represent a feature either just below or just above the slab top. The tilt direction calculated for this interface is 298°/118°, approximately northwest, near parallel to the direction of subduction, or southeast. This feature could plausibly be continuous with the ~40 km interface at CNP (Fig. 5b), given that its tilt direction could be consistent with NW-

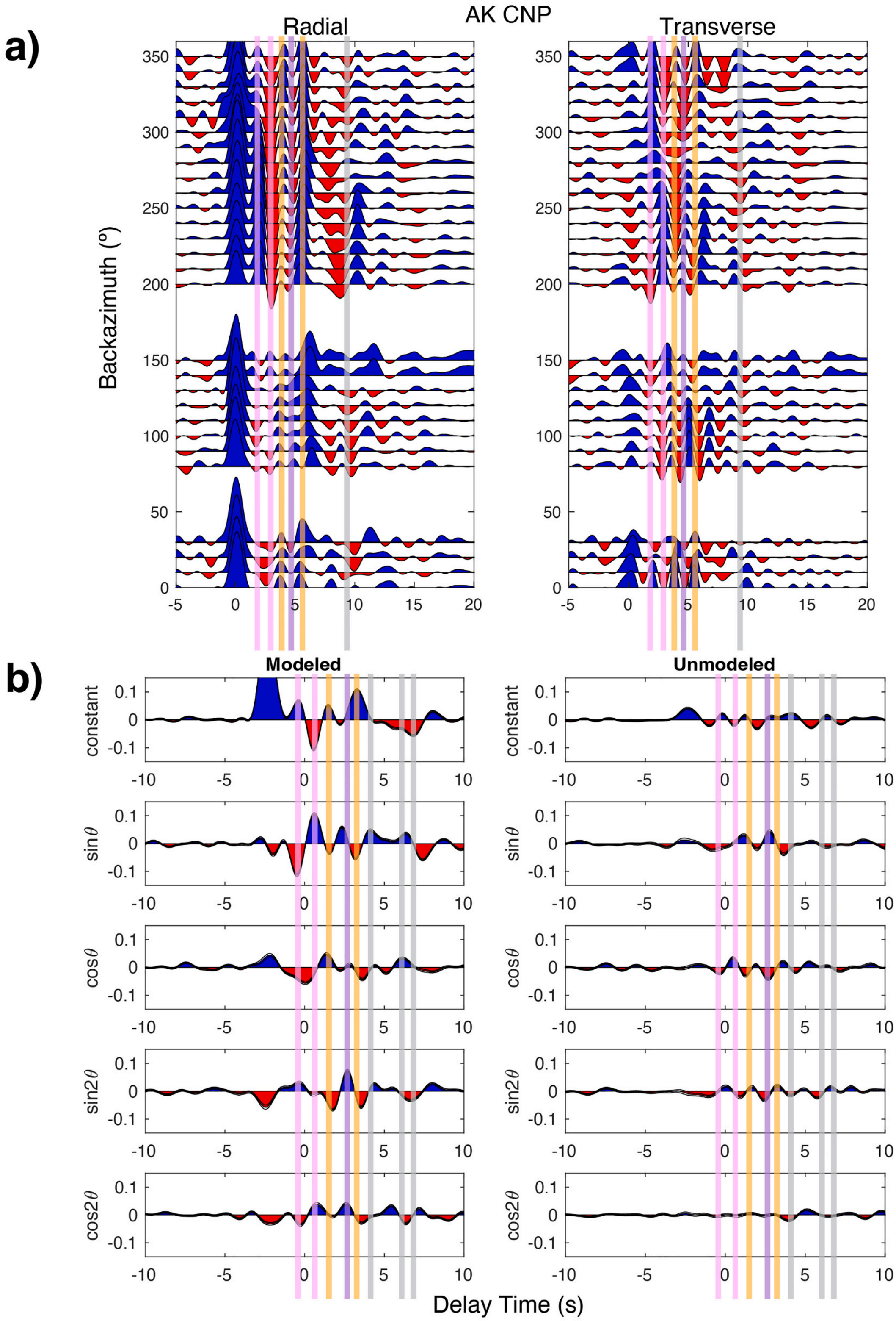

Fig. 5. a) Radial (left panel) and transverse (right panel) RFs for AK CNP sorted into backazimuthal bins and stacked. 0 s is the surface. b) Modeled (left set of panels) and unmodeled (right set of panels) harmonic decomposition RF gathers for AK CNP. The traces above and below the main trace in each panel are the bootstrapped error estimates. We show ten panels total in b), five for the modeled traces and five for the corresponding unmodeled traces. The top panel is the constant term, the second two panels are the $k = 1$ terms, and the bottom two panels are the $k = 2$ terms (see text for further details on modeled vs unmodeled traces, and k terms). 0 s is migrated to 20 km depth. Throughout the figure, arrivals with the same polarity as the direct P wave arrival are colored blue, and those with the opposite polarity are colored red. The overriding plate Moho and slab Moho are marked in orange, overriding plate interfaces are marked in pink, mantle wedge interfaces are marked in purple, and interfaces beneath the slab Moho are marked in gray. (For interpretation of the references to color in this figure legend, the reader is referred to the web version of this article.)

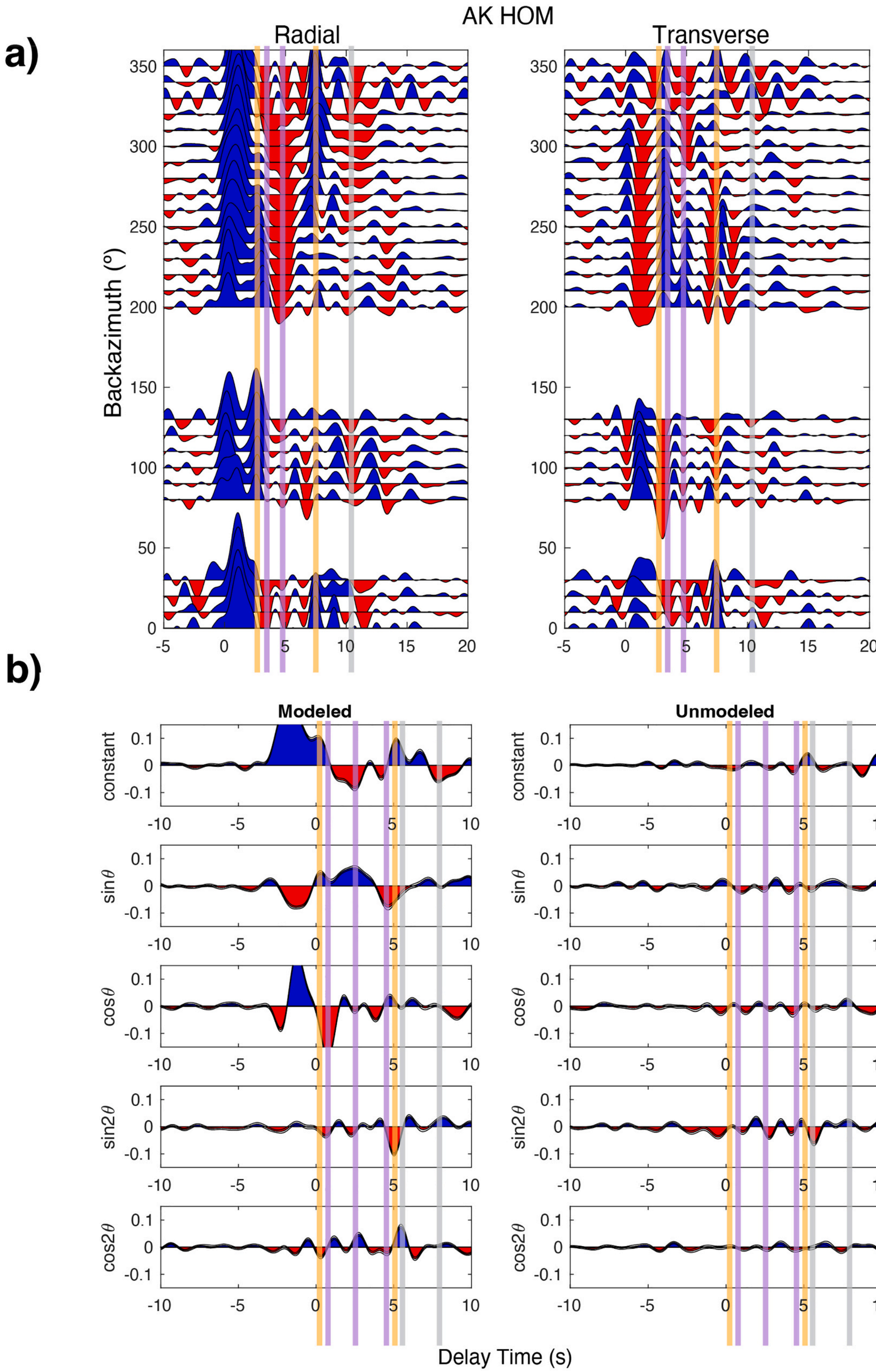

Fig. 6. Receiver function gathers for station AK HOM, with the same plotting conventions as Fig. 5.

SE anisotropy there, although here the orientation is obtained from the $k = 1$ terms while at CNP it is inferred from the $k = 2$ terms, the latter of which are associated with a 90° ambiguity (as it is unknown whether they are associated with the top or bottom of an anisotropic layer, or with fast or slow axes of symmetry). Just beneath the slab Moho, there is a positive pulse on the cos(2θ) term (Fig. 6b), indicative of an anisotropic interface associated with an approximately N-S or E-W fast orientation within the slab lithosphere itself. At ~95 km, there is a

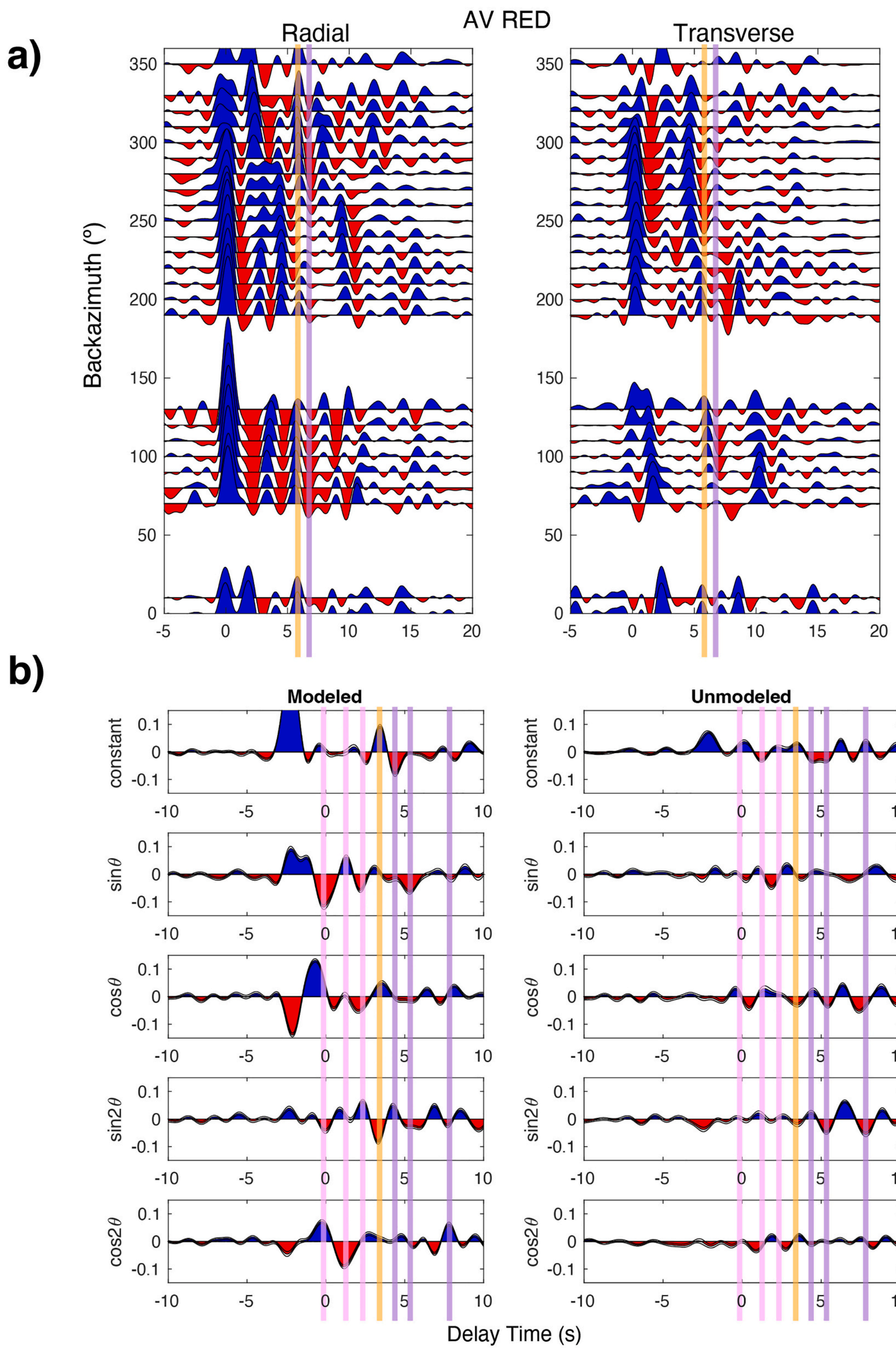

Fig. 7. Receiver function gathers for station AV RED, with the same plotting conventions as Fig. 5.

constant-term velocity decrease that could be associated with the base of the slab, implying a slab thickness of ~30 km.

Again assuming that the crust of the subducting slab is 6–8 km thick, the inferred slab Moho depth suggests that the slab top is located at ~60–65 km. Thus, interfaces between ~20 km and ~60–65 km can be attributed to mantle wedge structures. For this station, we infer the presence of two mantle wedge interfaces (Fig. 6). The first of these is associated with a large, negative cos(θ) pulse just beneath the overriding plate Moho at ~25 km. The tilt direction calculated for this interface is 172°/352°, approximately south or north. The second is a velocity decrease at ~40 km, which is associated with energy mostly on the sin (θ) component; the tilt axis here is 286°/106°, approximately northwest

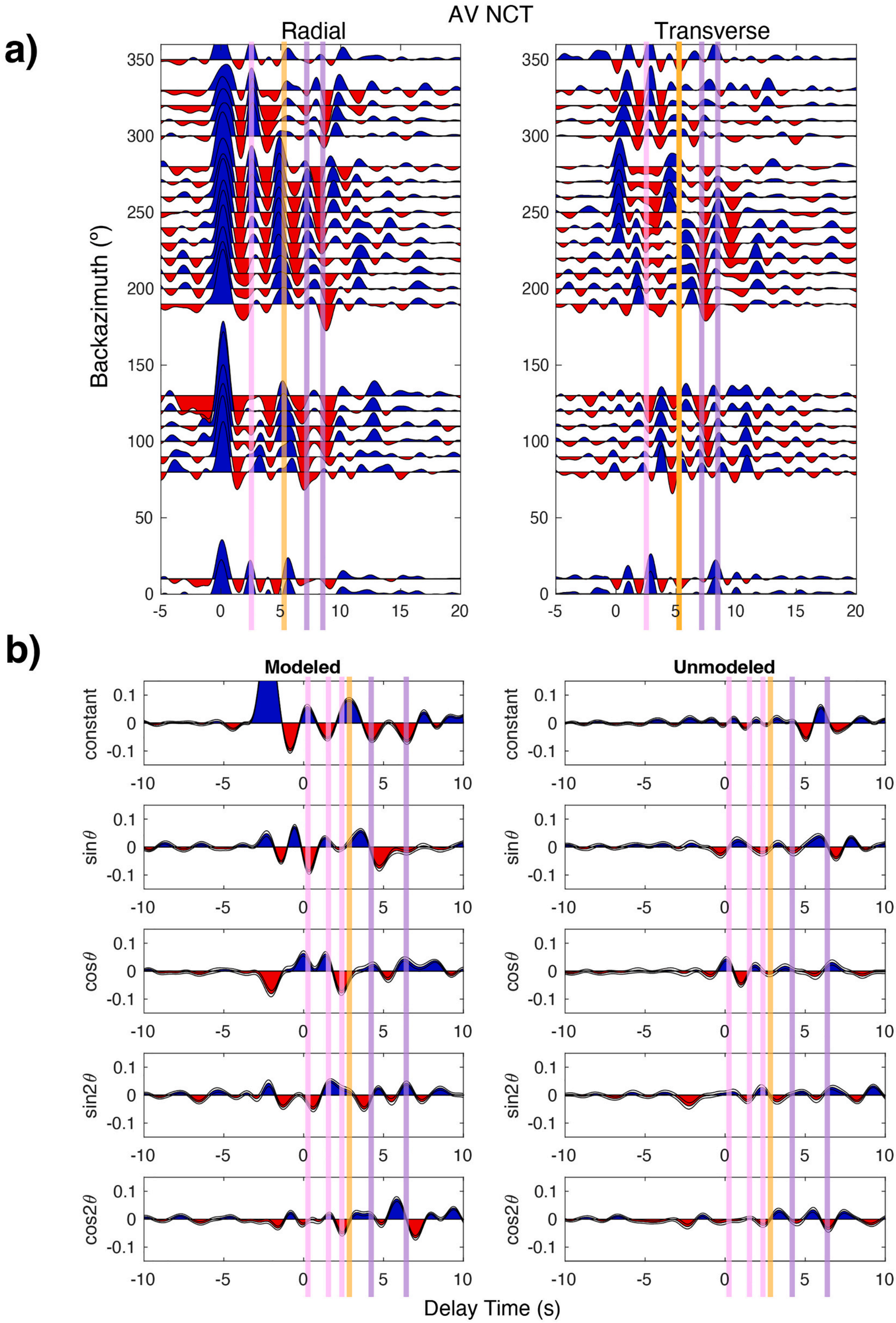

Fig. 8. Receiver function gathers for station AV NCT, with the same plotting conventions as Fig. 5.

or southeast. The presence of some signal on the cos(2θ) term at delay times associated with both of these interfaces indicates that they are likely associated with anisotropy.

3.1.3. AV RED

Station RED (Fig. 7) is located ~415 km from the trench, on or near the volcanic arc. We interpret the most prominent constant-term pulse, at roughly 6 s after the main P arrival, as corresponding to the continental Moho. This interface is located at ~50 km depth and is associated with a prominent, negative pulse on the sin(2θ) term, indicating anisotropy. It is evident from both the backazimuthal gathers (Fig. 7a) and from the harmonic decomposition (Fig. 7b) that there is significant intracrustal layering, with prominent pulses on the non-constant harmonic decomposition terms indicating the presence of significant anisotropy in the crust. Specifically, we identify an interface with a negative sin(θ) pulse and positive cos(2θ) pulse at ~20 km, and an interface with a positive sin(θ) pulse and negative cos(2θ) pulse at ~30 km. Because the $k = 2$ term energy is mainly on the cos(2θ) component for both interfaces (although the sign is different) and there is no prominent constant term energy associated with them, these could plausibly correspond to the top and bottom of a layer of anisotropy within the crust, with a north-south fast orientation or east-west slow orientation. The calculated tilt axes for these interfaces are 299°/119°, approximately northwest or southeast, and 85°/265°, approximately east or west, but it is important to note that the calculation for the first tilt direction may be impacted by the slightly shallower cos(θ) pulse. Given the strong sin(θ) signal, we suggest that an orientation closer to east-west is more likely. Taken together, the harmonic decomposition results thus suggest the presence of an anisotropic layer with a west-dipping fast axis or an east-dipping slow axis. A third intracrustal feature is associated with a positive sin(2θ) pulse at ~40 km, implying anisotropy. There is also energy on the $k = 1$ terms at this depth, but the unmodeled energy around this delay time is significant enough in amplitude to suggest that interpreting these pulses may be unreliable (Fig. 7). Anisotropic layers within the crust may reflect crustal deformation within the overriding plate itself. Alternatively, because this station is located at the volcanic arc, an anisotropic layer may correspond to layering or alignment of partial melt within the crust.

We also identified interfaces beneath RED at depths greater than that of the overriding plate Moho at ~50 km depth. We identify three interfaces of interest (Fig. 7); we interpret each of these as lying within the mantle wedge, as we do not see evidence for a clear arrival from the subducting slab Moho at this station. The first is an isotropic velocity decrease, perhaps corresponding to the top of a low-velocity layer within the mantle wedge (e.g., Wirth and Long, 2012; Nikulin et al., 2012), located below the overriding plate Moho at ~60 km. The second is associated with a negative sin(θ) pulse, indicating a dipping and/or anisotropic interface, at ~70 km. We did not calculate a tilt direction for this interface because while the sin(θ) signal is strong, the unmodeled cos(θ) signal at this delay time is relatively large, suggesting that the structure may not be simple enough to estimate a tilt direction using our approach. However, the strength of the sin(θ) signal does imply a significant contribution from a source with east- or west-dipping anisotropy. The final mantle wedge interface we interpret is associated with a positive cos(2θ) pulse at ~95 km, indicating the presence of anisotropy at this depth.

3.1.4. AV NCT

Station NCT is 435 km from the trench, and, like RED, is located close to the volcanic arc. Similar to station RED, NCT exhibits evidence for a clear Moho pulse corresponding to a depth of ~50 km (Fig. 8). As with RED, we do not find convincing evidence for a converted phase arrival from the slab Moho beneath this station. We do observe another positive pulse at ~20 km that covers the full backazimuthal range following the direct P arrival (Fig. 8a), but given NCT's proximity to RED and this station's location on the arc, it seems more likely that the ~50 km interface is the overriding plate Moho, and the ~20 km interface is an intra-crustal feature. The intracrustal interface is associated with strong $k = 1$ terms, and the calculated tilt direction is 301°/121°, approximately northwest or southeast, parallel to the direction of subduction (trench-normal). In addition to this ~20 km interface, we interpret three other intra-crustal interfaces (Fig. 8). The first expresses itself as a positive sin(θ) pulse at ~15 km, whose tilt direction is 76°/256°, approximately east or west. The second involves a velocity decrease at ~35 km, associated with a positive cos(θ) pulse and a positive sin(2θ) pulse; the tilt direction for this interface is 205°/25°, approximately south-southwest or north-northeast, and the energy on the sin(2θ) component would support a southwest or northeast orientation for anisotropy. The third interface, at ~40 km, is associated with a large, negative cos(θ) pulse, as well as a negative cos(2θ) pulse; this suggests that this interface likely has an anisotropic component. The tilt direction for this interface is 185°/5°, approximately north or south.

Within the mantle wedge, we identify two features of interest (Fig. 8). The first is a velocity decrease at ~60 km with a positive sin(θ) pulse just above it at ~55 km and a negative sin(θ) pulse just below it at ~65 km. The tilt directions for the sin(θ) pulses are 82°/262° and 279°/99°, both suggesting tilt directions approximately east or west. If these are taken to represent the top and bottom of an anisotropic layer, this would suggest approximately east-dipping anisotropy for a fast axis, or west-dipping anisotropy for a slow axis (see Fig. 3b). These may be consistent with the sin(θ) pulse at ~70 km beneath RED, although a tilt direction was not calculated for this interface as discussed above. This negative velocity gradient interface is also at the same depth (~55 km) as a similar negative interface inferred in the mantle wedge beneath RED, so this could represent the top of a continuous low-velocity feature in the mantle wedge. Second, there is an interface with an inferred large decrease in velocity at ~80 km, with a positive cos(2θ) pulse directly above it and a negative cos(2θ) pulse directly below it. These interfaces provide strong evidence of anisotropy in the sub-arc mantle.

3.2. Yakutat transect

For the Yakutat stations (Figs. 9-12), we find considerable complexity in the character of the RF gathers, with pulses often exhibiting polarity flips (or significant variations in amplitude) as a function of backazimuth on the radial component RFs. As discussed further below, this complexity likely reflects layered deformation and significant lateral heterogeneity within the flat slab region. The level of complexity of the RF gathers for the Yakutat stations means that confidently interpreting interfaces as either the overriding plate or slab Moho is somewhat challenging. This is also complicated by the fact that we may not necessarily expect to see the continental Moho as a positive arrival; for instance, there is evidence for a low-velocity layer directly above the subducting slab in the megathrust region (e.g. Kim et al., 2014; Mann et al., 2022). Nonetheless, we use this as a starting point for our interpretations, and discuss other plausible interpretations where appropriate. We primarily base our Moho interpretations on the constant terms of the harmonic decomposition gathers as these are more straightforward to interpret, although we label these interfaces on the backazimuthal gathers as well.

3.2.1. AK HIN

The closest station to the trench (155 km) is HIN. At this station, we identify a positive pulse at ~25 km as the likely continental Moho, and another positive pulse at ~40 km as the likely slab Moho (Fig. 9). The first of these pulses appears to flip polarity on the radial component of the backazimuthal gather (Fig. 9a), which suggests some complexity to this interface. Despite this complexity, the interpretation of the aforementioned pulses as the overriding plate and slab Moho, respectively, is more likely than another possible interpretation, which would place the continental Moho at ~40 km and the slab Moho at ~70 km. Our preferred interpretation, with the overriding plate Moho at ~25 km and the slab Moho at ~40 km, is consistent with a relatively shallow slab near the trench in the flat slab setting, and is also consistent with the interpreted overriding plate Moho depth for the adjacent station AK PWL (see section 3.2.2). This interpretation suggests that the top of the slab lies directly below the continental crust, given that the thickness of the downgoing slab crust is ~15 km (Worthington et al., 2012). The slab Moho signal appears to be associated with a positive sin(θ) pulse (Fig. 9b); the tilt direction calculated for this interface is 103°/283°, approximately east-southeast or west-northwest.

There are several anisotropic and/or dipping interfaces above the overriding plate Moho at ~25 km, which are likely indicative of layered deformation in the mid to lower crust. The first of these is associated with a very strong, positive cos(θ) pulse at ~15 km. Its tilt direction is 348°/168°, approximately north-northwest or south-southeast. There is

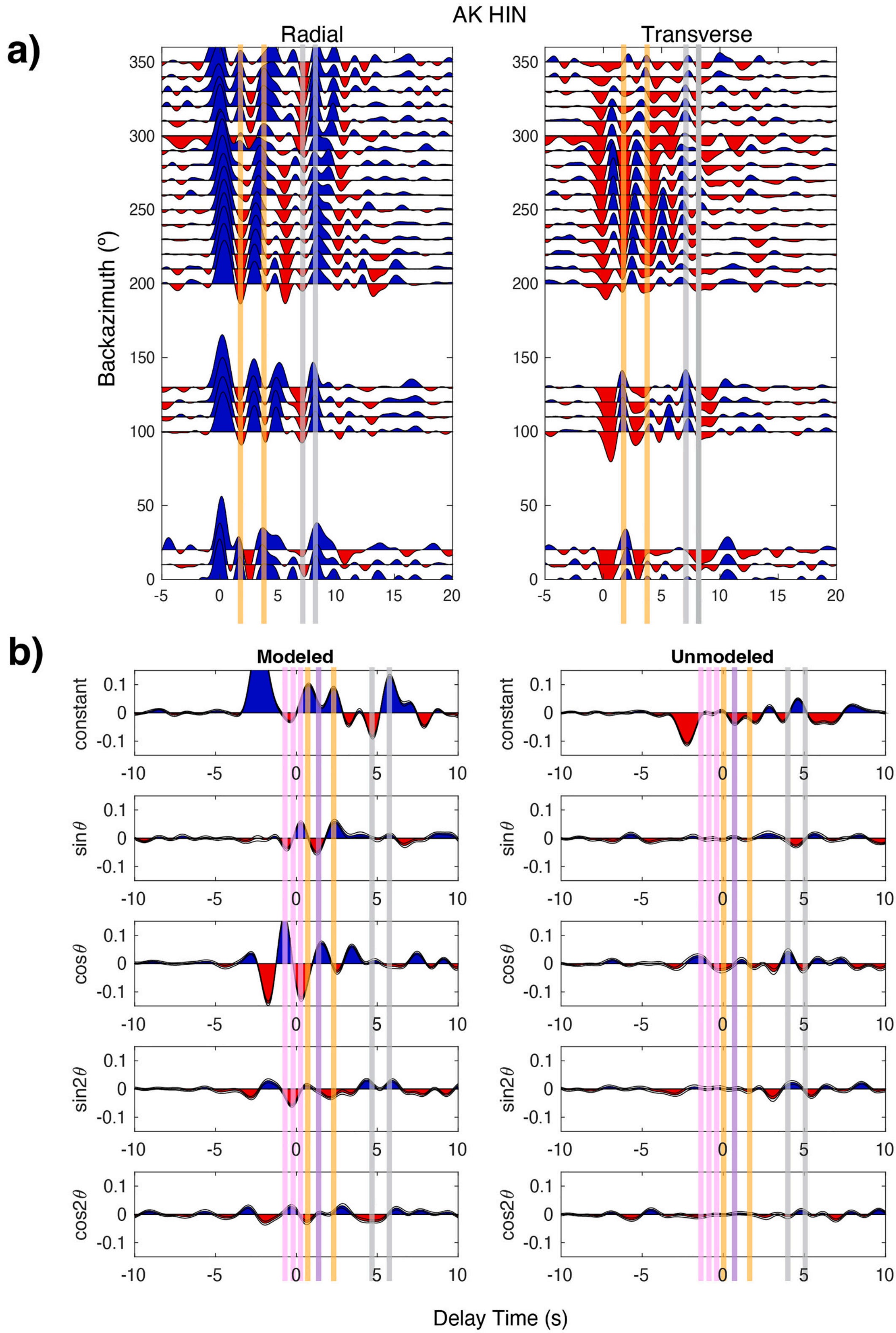

Fig. 9. Receiver function gathers for station AK HIN, with the same plotting conventions as Fig. 5.

another strong cos(θ) pulse just above the continental Moho at ~20 km, whose tilt direction is 156°/336°, similar in orientation to the shallower (~15 km) pulse. These two pulses are each associated with smaller sin (θ) components, and may represent the top and bottom of an anisotropic layer; if this is the case, the signal polarities would suggest a northwest-dipping fast axis or a southeast-dipping slow axis (see Fig. 3a,b). Between the ~15 km and ~20 km interfaces, there is a negative pulse on the sin(2θ) component (Fig. 9b). We identify one interface between the overriding plate Moho and slab Moho at ~30 km, associated with strong $k = 1$ terms (both sin(θ) and cos(θ); Fig. 9b). If the slab crustal thickness here is ~15 km (Worthington et al., 2012), then the slab top should lie at ~25 km; we infer, therefore, that this feature lies within the crust of the

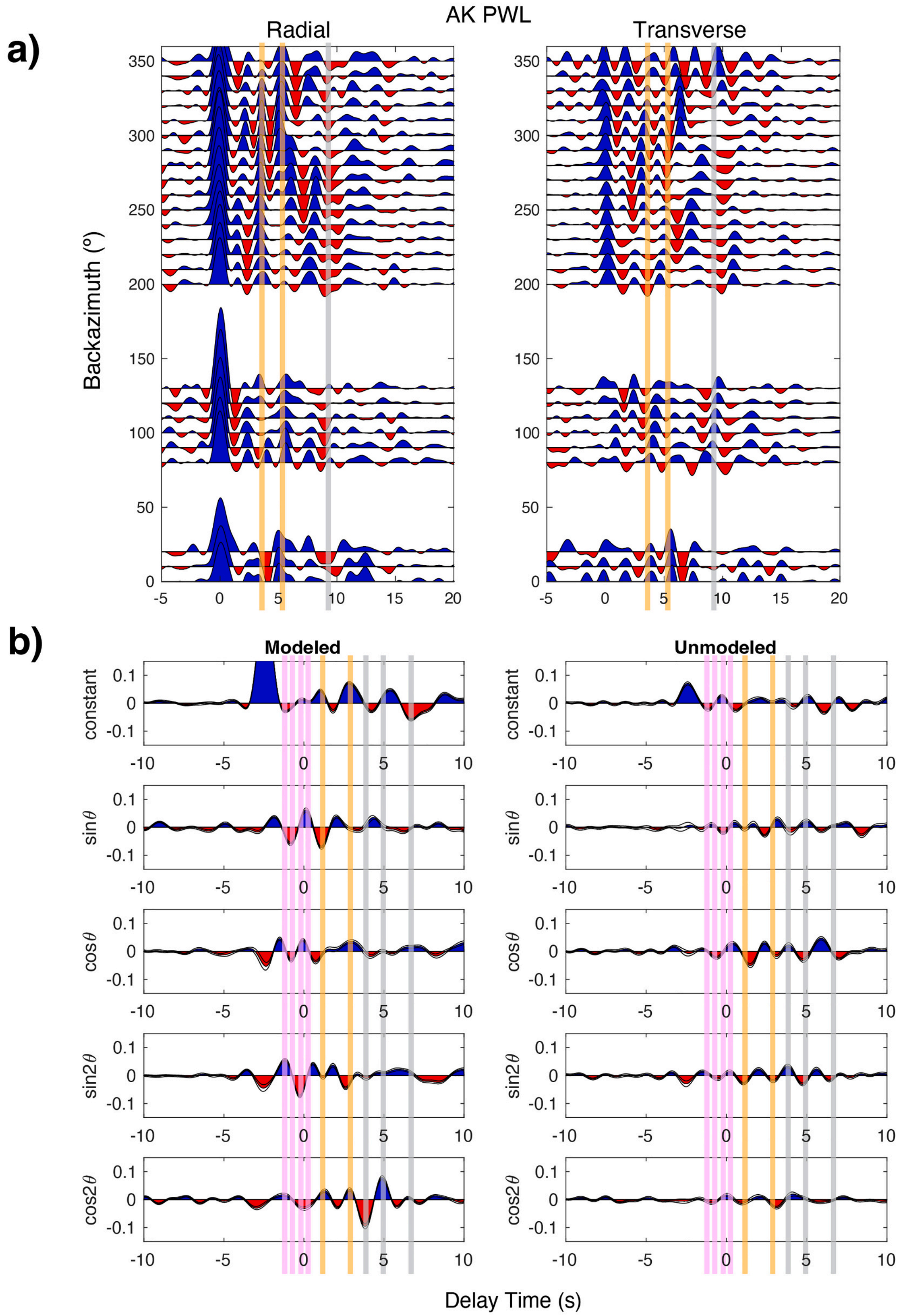

Fig. 10. Receiver function gathers for station AK PWL, with the same plotting conventions as Fig. 5.

downgoing flat slab, or could be associated with the slab top. Its estimated tilt direction is 312°/132°, similar to the orientations of the other two features for which tilt directions were calculated beneath this station; all tilt directions are near subduction-parallel. Beneath the overriding plate Moho, we identify two significant impedance contrasts within the slab mantle lithosphere (Fig. 9a), including a velocity decrease at ~60 km and a velocity increase at ~70 km.

3.2.2. *AK PWL*

Station PWL is ~255 km from the trench. Our preferred interpretation suggests that the overriding plate Moho lies at depth ~30 km, and the slab Moho at ~45 km (Fig. 10). The inferred continental Moho is also associated with a negative cos(θ) pulse (Fig. 10b), suggesting a dipping and/or anisotropic Moho, with a calculated tilt direction of 260°/80°, approximately west-southwest or east-northeast. Within the continental

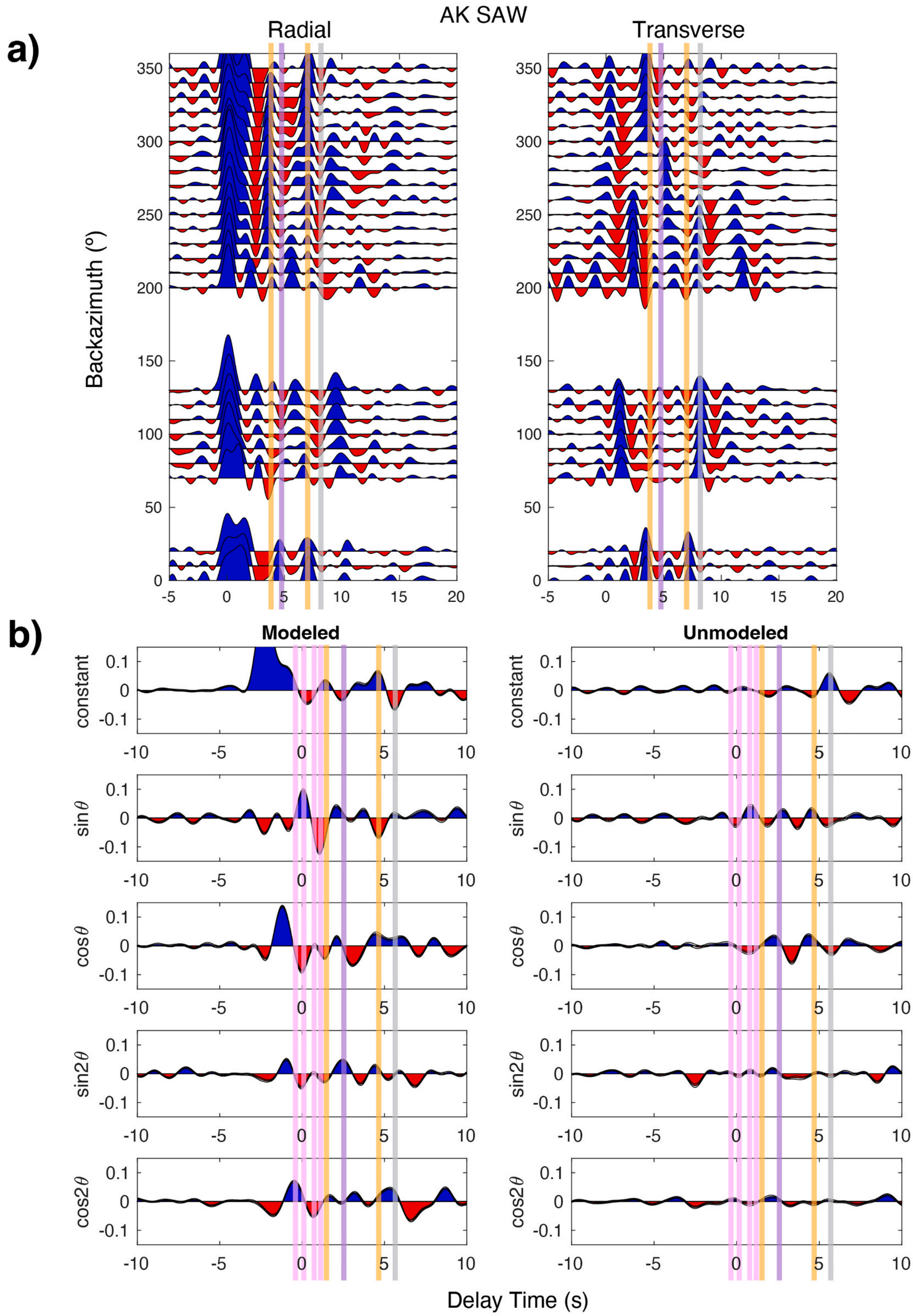

Fig. 11. Receiver function gathers for station AK SAW, with the same plotting conventions as Fig. 5.

crust, we interpret several dipping and/or anisotropic interfaces. The shallowest of these is associated with a negative sin(θ) pulse at ~15 km with a tilt direction of 242°/62°, nearly trench-parallel. Directly above and below this interface, we see evidence for a positive and a negative sin(2θ) pulse (Fig. 10b), respectively; these suggest the presence of anisotropic layer within the continental crust. Just beneath the negative sin(2θ) pulse is a positive sin(θ) pulse at ~20 km (Fig. 10b) with a tilt direction of 65°/245°, again similar to the two tilt directions calculated for other interfaces beneath this station.

If the slab crustal thickness here is ~15 km, the slab top should be at ~30 km, suggesting that the top of the slab lies just below the continental crust, with little or no mantle material separating the two crustal bodies, similar to our interpretation at adjacent station HIN. Beneath the slab Moho at ~45 km, we infer additional interfaces. Specifically, we observe two high-amplitude, adjacent cos(2θ) pulses, one negative and one positive, at ~55 km and ~60 km, respectively (Fig. 10b). These

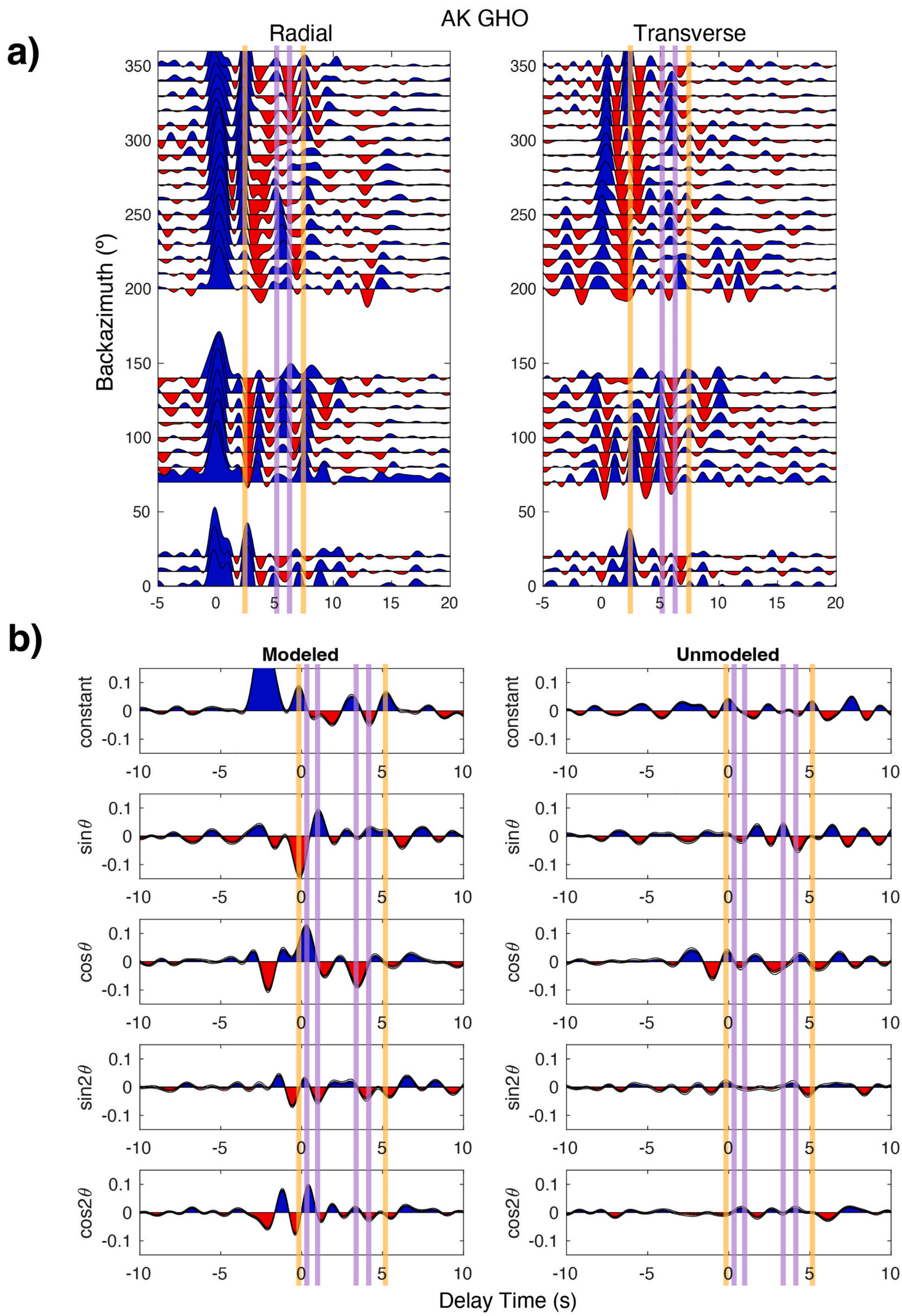

Fig. 12. Receiver function gathers for station AK GHO, with the same plotting conventions as Fig. 5.

prominent signals likely reflect anisotropy within the flat slab mantle lithosphere. Finally, beneath these interfaces, we observe a velocity decrease at ~75 km (Fig. 10), which may plausibly represent the base of the slab lithosphere.

3.2.3. AK SAW

Station SAW is located ~340 km from the trench. We infer that the overriding plate Moho is located at a depth of ~30 km, comparable to our inferred crustal thicknesses beneath both HIN and PWL, and that the slab Moho lies at a depth of ~60 km (Fig. 11). As at the other Yakutat stations, there are several dipping and/or anisotropic interfaces within the continental crust that may be linked to deformation of the overriding plate. The first is a prominent feature on the $k = 1$ terms (a positive sin (θ) pulse associated with a negative cos(θ) pulse) at a depth of ~20 km

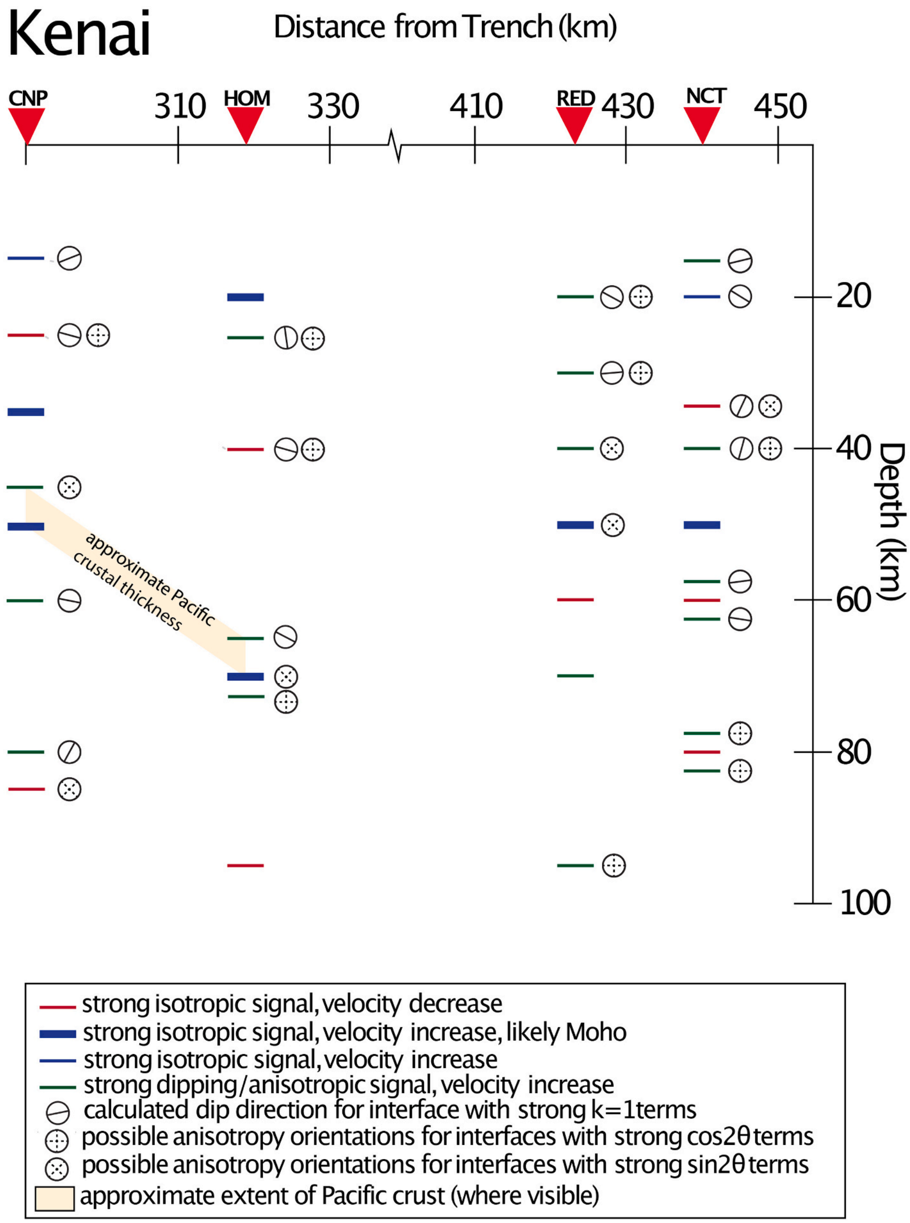

Fig. 13. Vertical cross section showing interfaces of interest along the Kenai transect. Interfaces with strong isotropic signals are marked with blue (for positive arrivals) or red (for negative arrivals). Interfaces with strong $k = 1$ or $k = 2$ arrivals that lack a strong isotropic arrival are indicated by green lines. Circles indicate dip direction or anisotropic orientation in map view (top = north). (For interpretation of the references to color in this figure legend, the reader is referred to the web version of this article.)

(Fig. 11b). The calculated tilt direction for this interface is 132°/312°, approximately northwest or southeast, and parallel to the direction of subduction (trench-normal). On either side of this interface, we identify $\cos(2\theta)$ pulses, a positive pulse above and a negative pulse below, suggesting an anisotropic layer in the mid- to lower crust. We also observe another interface associated with a large, negative $\sin(\theta)$ pulse just above the continental Moho (Fig. 11b); the tilt direction for this interface is 262°/82°, approximately east or west. Between the overriding plate Moho and the slab Moho, there is significant unmodeled energy on the $k = 1$ components of the harmonic decomposition gather, suggesting that the mantle wedge and slab crust may be complex and exhibit significant lateral variability in their structure, and indicating that interpretation of these pulses is uncertain. There is, however, significant energy on the $k = 2$ components in this depth range, suggesting the presence of multiple anisotropic interfaces above and within the flat slab (Fig. 11b). Specifically, the velocity decrease at ~40 km may correspond to the top of the subducting slab; this interface is also associated with a positive pulse on the $\sin(2\theta)$ component, suggesting horizontal anisotropy. If this is indeed the slab top, that would suggest a slab crustal thickness of ~20 km beneath SAW, slightly thicker than what is inferred elsewhere for the subducting Yakutat terrane. In the slab mantle lithosphere beneath SAW, we observe a velocity decrease at ~70 km that is associated with energy on the $\sin(2\theta)$ component. Significant signal on the $\cos(2\theta)$ component is also present for the time range corresponding to 70–100 km depth, suggesting multiple layers of anisotropy within the lithospheric mantle of the Yakutat slab (Fig. 11b).

3.2.4. AK GHO

Beneath station GHO, located ~380 km from the trench, we infer that the overriding plate Moho is at a depth of ~20 km, and the slab Moho at a depth ~65 km (Fig. 12). Given the complexity of the RF gathers beneath this station, there are several other possible

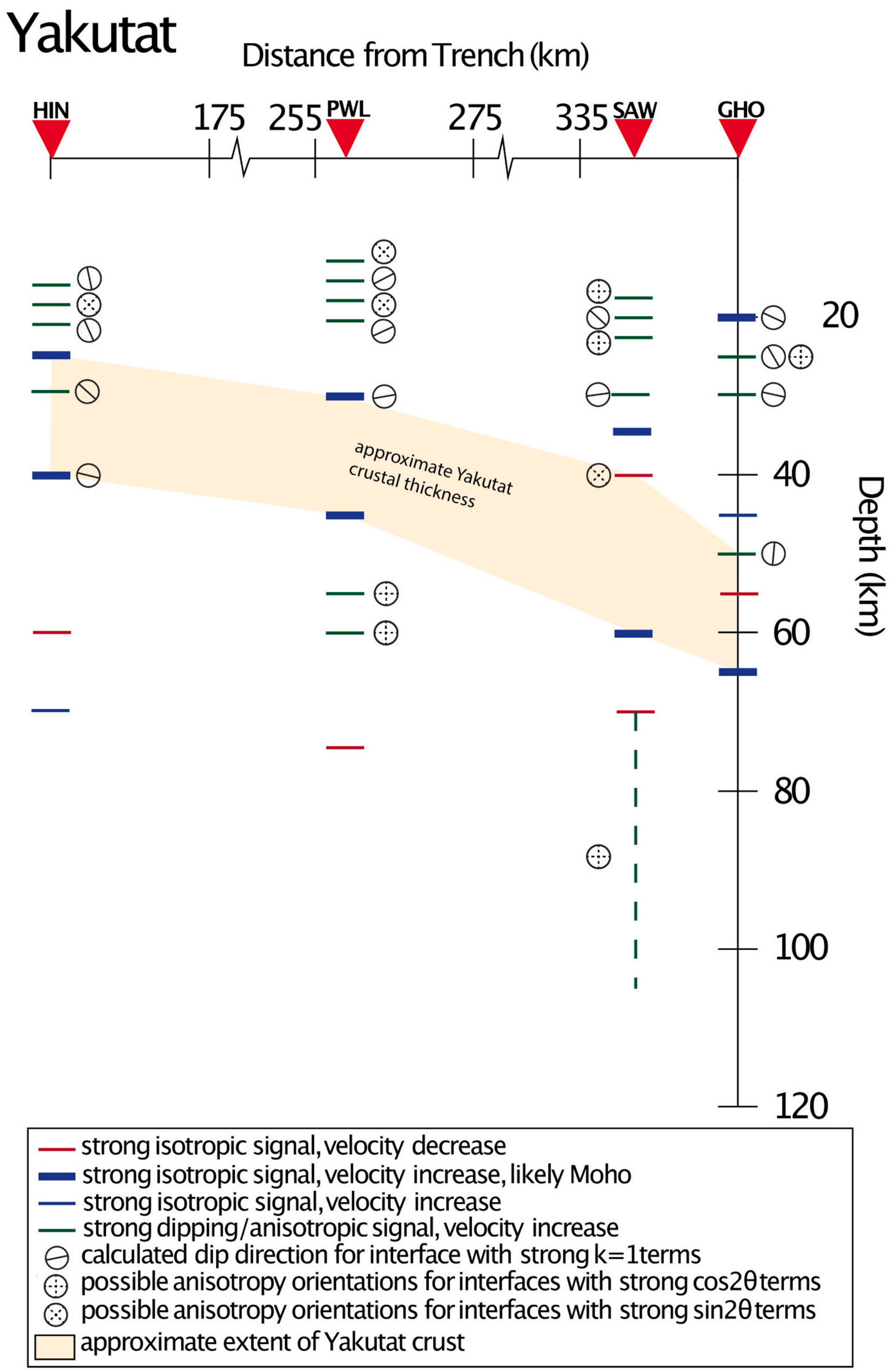

Fig. 14. As Fig. 13, but for the Yakutat transect.

interpretations for the locations of the slab and overriding plate Moho, but we favor these interpretations as they are the most consistent with structures observed elsewhere along the transect. Specifically, there are three positive pulses on the constant term of the harmonic decomposition that could feasibly be interpreted as a Moho signal, at ~20 km, ~45 km, and ~65 km (Fig. 12). We suggest that the slab Moho most likely lies at ~65 km depth; if it were located at ~45 km, this imply a change in slab Moho depth of ~15 km over <40 km laterally. While this not completely implausible given the complexity of the flat slab system, we nonetheless suggest that it is not the most likely scenario. This leaves either the ~20 km interface or the ~45 km interface as plausible candidates for the continental Moho. We again suggest that the smaller change in Moho depth between SAW and GHO (~30 km to ~20 km) is the more likely interpretation given the proximity of these stations. The observed consistency of the non-constant terms on the harmonic decomposition gather among stations PWL (Fig. 10b), SAW (Fig. 11b), and GHO (Fig. 12b) also favors a ~20 km overriding plate Moho beneath GHO. Specifically, the Moho picks at PWL and SAW are each associated with a negative $\sin(\theta)$ term; the ~20 km interface at GHO also exhibits this feature. We acknowledge that other interpretations are plausible, however, including the possibility the Moho beneath GHO actually lies between these two observed interfaces, and for some reason it does not appear as a strong positive arrival.

The interface we interpret as the likely overriding plate Moho is also

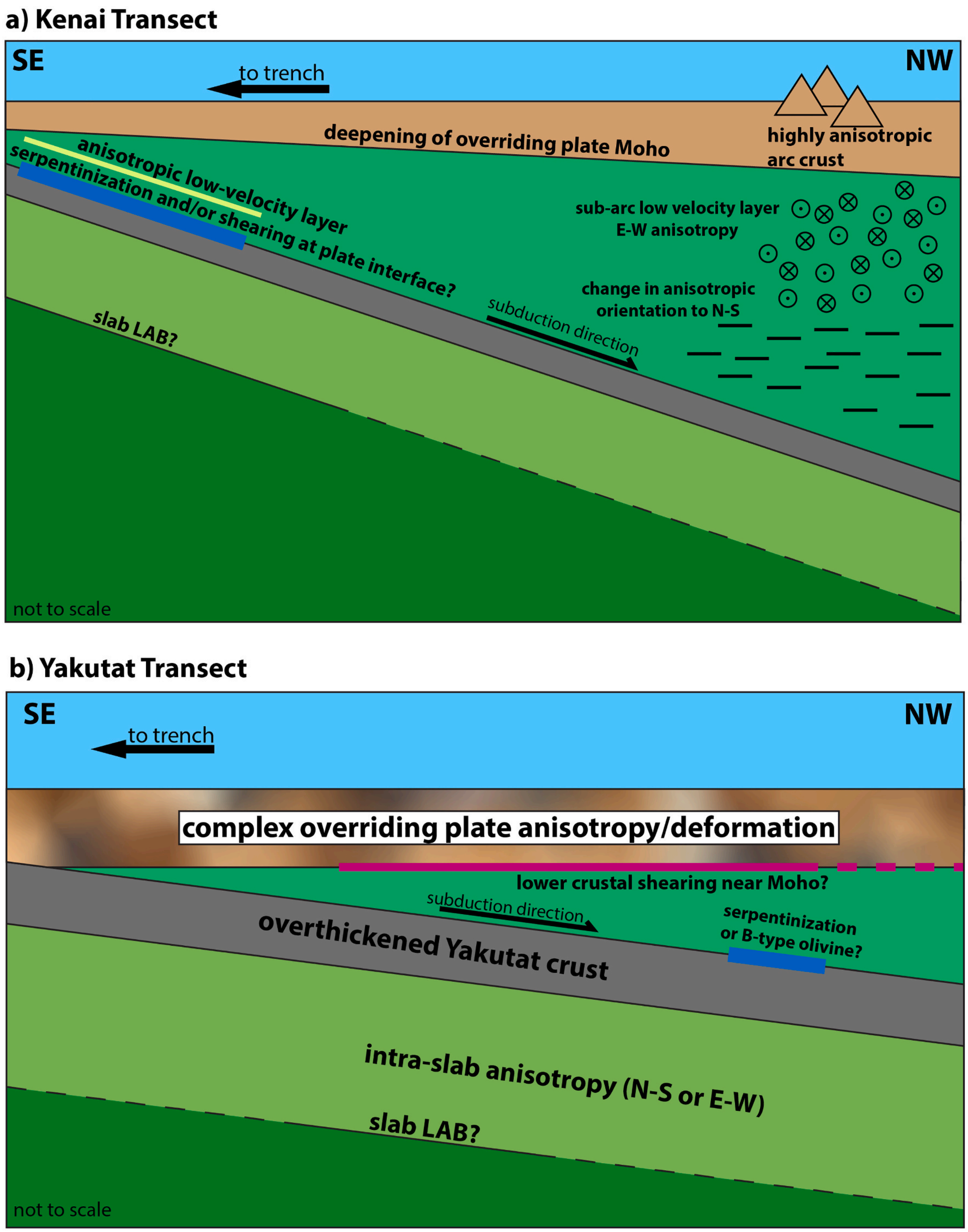

Fig. 15. Cartoon interpretations for the normally-dipping (a) and flat slab (b) transects.

associated with a large sin(θ) term (Fig. 12b), for which the tilt direction is 295°/115°, approximately northwest or southeast. The velocity decrease between the continental Moho and the slab Moho at ~55 km could plausibly correspond to the slab top, but this would imply that the subducting crust thins by ~50% between SAW and GHO, which we consider to be unlikely. Instead, we suggest that the slab top may be associated with the large, negative cos(θ) pulse at ~50 km (tilt direction of 185°/5°, approximately north or south), and that the ~55 km velocity decrease is an intra-slab feature. If our preferred interpretation is correct, then features located between ~20 km and ~50 km lie within the volume of mantle between the slab top and the overriding plate crust (the "mantle wedge" in a normally dipping subduction zone, although this term is not always applied in flat slab systems; e.g., Eakin et al., 2014). We infer several anisotropic and/or dipping interfaces within this mantle layer beneath station GHO. There is an interface at ~25 km depth with a large, positive cos(θ) term as well as a large, positive cos(2θ) term. The tilt direction for this interface is 330°/150°, approximately northwest or southeast, and parallel to the subduction direction. At ~30 km depth, there is an interface associated with a large, positive sin(θ) term, whose tilt direction is 102°/282°, approximately east-southeast or west-northwest. The presence of significant energy on the $k = 2$ terms in the depth range of the aforementioned interfaces indicates that they are strongly anisotropic, likely as a result of overriding plate deformation. It is difficult to confidently identify and characterize interfaces beneath the slab Moho at GHO, as the unmodeled terms become significant below this depth. Additionally, an important caveat in interpreting tilt directions calculated for this station is that many of the $k = 1$ pulses are relatively closely spaced (Fig. 12b), such that the tilt direction calculated for a given pulse is likely influenced by the shoulder of a pulse directly above or below it.

4. Discussion

The interpretations detailed above are illustrated in schematic form in Figs. 13 and 14 to allow for a collective interpretation of the stations included in each transect. These diagrams show the station locations and the depths and likely interpretations of significant interfaces, along with the tilt directions calculated from the $k = 1$ terms and approximate orientations of anisotropy (i.e., NE-SW/NW-SE or N-S/E-W) obtained from the $k = 2$ terms. Cartoon sketches detailing our major interpretations for both transects are shown in Fig. 15.

4.1. Isotropic structure

4.1.1. Continental crust thickness

The thickness of the continental crust beneath the Kenai transect generally increases with increasing distance from the trench; the thicknesses at CNP and HOM are ~35 km and ~20 km, respectively, while the thickness beneath the arc at RED and NCT is ~50 km. Beneath the Yakutat transect, however, the thickness of the continental crust appears to be relatively consistent along the length of the transect at ~25–30 km. Estimates of the thickness of the continental crust along the southern coast are in broad agreement with previous studies (e.g., Miller et al., 2018; Zhang et al., 2019; Gama et al., 2021, 2022). Although Zhang et al. (2019) infer thicker crust overall, the thicknesses shown by Miller et al. (2018) and Gama et al. (2022) can be somewhat variable locally, and our values appear to be in agreement with theirs in general. A notable exception, however, is GHO, where we suggest that ~20 km is the more likely depth of the overriding plate Moho, while Miller et al. (2018) suggest it is closer to ~40 km. Conversely, the Sp common conversion point stacking study of Gama et al. (2022) places the Moho beneath GHO at ~15 km, much closer to our ~20 km estimate. Gama et al. (2022) point out that such discrepancies may be related to different criteria for identifying the Moho arrival. As discussed in section 3.2.4, our Moho pick is partly informed by the proximity of GHO to neighboring station SAW, and placing the Moho at ~45 km, the next significant positive pulse, would suggest an even larger change in crustal thickness over <40 km. However, as will be discussed below, it is also possible that the depth of the Moho beneath GHO is similar to that of the Moho beneath the other Yakutat stations, and for some reason it does not appear as a prominent arrival on our RF gathers.

Another possible interpretation of our continental Moho depth estimates for the Yakutat transect, particularly beneath HIN and PWL, is that they are actually associated with the bottom of the slab top low-velocity layer imaged by Kim et al. (2014) and Mann et al. (2022). Both the continental Moho and the base of a low-velocity layer would appear as a positive velocity gradient with depth, and the depth we infer for the continental Moho beneath these stations (~25–30 km) is similar to the depth to the bottom of the low-velocity layer observed by Kim et al. (2014) and Mann et al. (2022). We do not observe a clear, high-amplitude negative arrival on the radial RFs that could be associated with the top of such a low-velocity layer, however, so it is not clear whether we are truly imaging this feature.

4.1.2. Slab geometry

The slab Moho beneath the Kenai transect deepens significantly between CNP and HOM, and is not identified beneath RED and NCT. Given the depths of the slab Moho beneath CNP and HOM, and the dip angle they imply for the Pacific slab (~50°), the slab Moho is likely at depths deeper than those at which we interpret our RFs beneath RED and NCT. We note, however, that our dip estimate for the Pacific slab is steeper than what is inferred via tomography (~30–40°; Gou et al., 2019). We also compare our results to several sets of slab contours, including those from Li et al. (2013), the Slab2 model (Hayes et al., 2018), and Gou et al. (2019). The depth to the slab top indicated by our results is deeper than what is suggested by Slab2 (Hayes et al., 2018) and by Gou et al. (2019), who predict a slab top depth of ~40 km beneath the northwestern coast of the Kenai Peninsula, but appears to be in somewhat better agreement with Li et al. (2013), who predict a slab top depth of ~60 km in the same area; our results suggest that the slab top is ~45 km beneath CNP and ~65 km beneath HOM.

Beneath CNP and possibly HOM (depending on the estimated overriding plate Moho depth), there is evidence for a velocity decrease within the mantle wedge or the crust. This could be continuous with the velocity decrease imaged beneath RED and NCT, or they may have different origins (Fig. 13). This may suggest the presence of a low-velocity region within the mantle wedge, which has been inferred for other regions based on RF data (e.g., Wirth and Long, 2012; Nikulin et al., 2012). We infer a thickness of ~10 km for the Pacific plate crust, in general agreement with the 6–8 km thickness obtained by Kim et al. (2014); the slight difference between our estimate and the nominal average for oceanic crust likely reflects limitations in the resolution of our measurements, rather than a significant disparity. Relatively deep interfaces with velocity decreases beneath CNP and HOM (~85 and ~95 km, respectively), could be associated with the base of the slab and would imply a slab lithospheric thickness of 30–40 km, consistent with previous estimates of slab lithospheric estimates beneath Alaska of 30–60 km (Zhao et al., 1995; Eberhart-Phillips et al., 2006). The LAB depths estimated by Gama et al. (2022), however, are consistently deeper than our estimates by ~30–40 km. Thus, our results may instead suggest strong layering in the slab mantle lithosphere rather than imaging the base of the slab, although it is not immediately clear why such layering would be present.

Beneath the Yakutat transect, the slab Moho remains relatively shallow along the length of the transect, reaching a depth of only ~65 km beneath GHO, the farthest station from the trench; in the normally dipping segment, the slab Moho is at ~65 km beneath HOM, the second station from the trench. This highlights the dramatic difference in dip between the normally-dipping and flat slab segments. We infer that there is little or no mantle "wedge" present beneath the first two stations in the Yakutat transect, HIN and PWL, as the top of the subducting slab is inferred to be just below the continental Moho (~25–30 km), given that the slab Moho beneath these two stations is at ~40–45 km. Further along the transect, beneath SAW and GHO, there appears to be a thicker layer of mantle present between the base of the overriding plate crust and the top of the slab, which in this section of the transect are at depths of ~30 km and ~ 50 km, respectively. The location of the shallowly-dipping slab beneath the Yakutat transect is also consistent with previous work; we suggest that the slab Moho ranges in depth from ~40–65 km moving down-dip along the transect. This is ~10 km deeper than what is observed by Mann et al. (2022) for the same region, and quite similar to what is observed by Kim et al. (2014), although we note that the region studied by Kim et al. (2014) is slightly farther west than our study area, and thus may have somewhat different slab geometry. The corresponding slab top depths for our Moho depth estimates range from ~25–50 km, ~5–20 km deeper than the estimates of Mann et al. (2022) (~15–30 km), the Slab2 model (Hayes et al., 2018) (17–34 km), and Kim et al. (2014) (20–45 km).

We also infer some heterogeneity in slab crustal and mantle wedge thickness. Overall, our results suggest a slab crustal thickness of ~15–20 km, within the range of previous estimates (Ferris et al., 2003; Rossi et al., 2006; Eberhart-Phillips et al., 2006; Worthington et al., 2012; Kim et al., 2014; Mann et al., 2022). Within the slab lithospheric mantle beneath HIN, there appear to be some significant impedance contrasts, perhaps implying complex structure within the slab mantle lithosphere (Fig. 14), although the processes that might lead to a strongly layered oceanic lithosphere are not immediately clear. We observe a clear velocity decrease at ~75 km depth beneath PWL; if this interface indeed represents the bottom of the slab lithosphere, this suggests a slab lithospheric thickness of ~45 km. This is also consistent with the 30–60 km lithospheric thickness estimated by Zhao et al. (1995) and Eberhart-Phillips et al. (2006) for the slab beneath Alaska, and is consistent with a thicker slab beneath the Yakutat transect than beneath the Kenai transect. Similar to the Kenai transect, however, the LAB depth estimated for this region by Gama et al. (2022) is ~25 km deeper than we observe beneath PWL, so the interfaces we observe may again be indicative of a complex intra-slab velocity structure instead of the base of the lithosphere.

4.2. Anisotropic structure

4.2.1. Kenai transect

Beneath the two stations closest to the trench, CNP and HOM, there is evidence for dipping and/or anisotropic features in the mantle wedge. The interface near the inferred slab top beneath CNP is associated with a $k = 2$ term, so it is almost certainly anisotropic. If it is assumed that this interface represents the top of a layer and is the result of fast axis alignment, the $k = 2$ signal suggests a N*E*-SW fast direction, approximately trench-parallel. Equivalently, this signal could also be indicative of trench-normal slow axis alignment (which would imply a trench-parallel fast direction). Two mineral fabrics are generally thought to produce trench-parallel fast directions: deformed serpentine (e.g., Katayama et al., 2009; Bezacier et al., 2010; Jung, 2011; McCormack et al., 2013; Wagner et al., 2013; Horn et al., 2020) and B-type olivine (e.g., Jung and Karato, 2001; Karato et al., 2008; Kneller et al., 2005, 2008; McCormack et al., 2013), both of which are thought to form under water-rich mantle conditions. For serpentine, the slow axis aligns perpendicular to the shear plane, and thus often perpendicular to the slab surface (Katayama et al., 2009); this would likely produce a trenchward-dipping slow axis signal. For B-olivine, the fast axis is perpendicular to deformation but in the shear plane (Jung and Karato, 2001), appearing as a trench-parallel fast axis. In this situation beneath CNP, the anisotropic signal occurs on the $k = 2$ terms, indicating approximately horizontally-oriented anisotropy. The corresponding interface beneath HOM is more closely associated with a $k = 1$ term, so in theory this could represent a dipping or anisotropic interface at the top of the slab. If the HOM interface is interpreted as an upper interface and is inferred to be associated with a slow symmetry axis, the tilt direction for the slow axis is southeast, approximately trenchward (see section 3.1.2). Thus, these signals could be associated with serpentinization of the mantle above the plate interface, if the interface beneath CNP is also interpreted as a result of slow axis alignment. We note, however, that the presence of serpentine should also lead to a negative velocity contrast, which is not observed (e.g. Bostock et al., 2002). Alternatively, if the HOM interface is interpreted as a result of fast axis alignment, the tilt direction for the anisotropy is approximately northwest, parallel to the subduction direction. In that case, if the anisotropic signal at CNP is associated with slab top serpentinization, it would not be continuous beneath HOM. Alternatively, if the interface beneath CNP is instead the bottom of an anisotropic layer, the fast direction would be oriented NW-SE and these two interfaces could be indicative of a layer of material experiencing subduction-parallel shearing near the surface of the slab. This scenario would rule out B-type olivine and serpentine, but could be associated with a different olivine alignment or with other sheared material at the slab top. A last possibility is that a trench-parallel fast direction beneath CNP is associated with B-type olivine and a trenchward-dipping slow axis beneath HOM is associated with serpentinization, which would suggest that this feature is not continuous between the two stations. In any case, these anisotropic signals are likely indicative of deformation at the slab top.

The ~15 km interface beneath CNP seems less likely to be the overriding plate Moho based on the backazimuthal gather (Fig. 5a) and previous studies on the thickness of the crust along the southern coast of Alaska (Miller et al., 2018; Zhang et al., 2019); however, if it is the Moho, this would suggest a continuous low-velocity feature in the mantle wedge beneath both CNP and HOM, with a generally consistent and approximately east-west oriented tilt direction (Fig. 13). Energy on the cos(2θ) term at both stations is indicative of anisotropy oriented either N-S or E-W. An E-W orientation would be somewhat more consistent with the tilt direction. However, because it is not clear whether this is a top or bottom interface, or if the anisotropy is due to the alignment of slow axes (more likely if this interface is crustal; e.g., Brownlee et al., 2017) or fast axes (more likely for a mantle interface), it is difficult to constrain the anisotropy based on the $k = 2$ terms. Regardless of the anisotropic orientation associated with the $k = 2$ terms, it seems most likely that such a mantle wedge feature could be a result of olivine fabric resulting from deformation. Deformation in the mantle wedge could produce anisotropy oriented in either direction, depending on whether the deformation results in B-type vs. A-, C-, or E-type fabrics (e.g., Long, 2013). It is also worth noting the possibility that the Moho at HOM is deeper than our preferred interpretation indicates, which would make this an intra-crustal interface. We note, however, that we do not observe evidence for another possible Moho interface on the backazimuthal gather or the constant term of the harmonic decomposition gather (Fig. 6), making this possibility less likely.

There is also anisotropy associated with the slab Moho beneath HOM, as well as just beneath it. The velocity increase inferred to correspond to the slab Moho is also associated with signal on the sin(2θ) term, but just below the slab Moho, there is energy on the cos(2θ) term, implying a likely change in anisotropic geometry between the oceanic crust and lithospheric mantle. There are also multiple dipping and/or anisotropic layers with varying orientations within the slab mantle lithosphere at CNP, which show a mix of orientations and thus imply heterogeneity within the slab lithospheric mantle. The ~60 km interface suggests an approximately east-west orientation, while the ~80 km interface is closer to NE-SW. As discussed in section 4.2.1, it is possible that the velocity decrease beneath CNP at ~85 km is associated with the base of the subducting slab, so the anisotropy inferred here could either be due to anisotropy within the slab lithosphere or in the sub-slab asthenospheric mantle, and would suggest a contrast in anisotropic geometry between them.

Beneath RED and NCT, we infer the presence of anisotropic structures in the overriding plate. The cos2(θ) pulses at ~20 and ~30 km beneath RED could represent the top and bottom of an anisotropic layer in the crust. For a slow axis alignment, which is expected for many crustal minerals (e.g., Brownlee et al., 2017), these results would suggest an east-west orientation, which is approximately consistent with the tilt directions calculated from the $k = 1$ terms at these interfaces. The shallower interfaces beneath NCT also exhibit tilt directions relatively close to east-west, but the ~35 km and ~40 km interfaces beneath NCT are different, closer to NE-SW (approximately trench-parallel), implying a change in geometry with depth. As these stations are located close to the volcanic arc, these structures could be related to deformation of the crustal column, the presence of aligned melt through a shape-preferred orientation (SPO) effect, or a combination thereof.

Schulte-Pelkum et al. (2020) carried out anisotropic receiver function analysis and characterized first-order signals throughout Alaska. They observe some of their strongest anisotropic/dipping signals in the south-central region where we carried out our study. For each station included in their study (which includes all eight stations in our transects), they estimate the strike and depth of the interface associated with the strongest dipping/anisotropic signal. Their results suggest that the largest dipping/anisotropic signal in this region originates in the crust, which is consistent with our harmonic decomposition results (Figs. 5b–8b). Beneath CNP, HOM, and RED, the depths of the maximum signals Schulte-Pelkum et al. (2020) observe are shallower than the depths at which we interpret our harmonic decomposition gathers, but beneath NCT we have directly comparable results; the strike they predict at ~15 km beneath NCT is approximately perpendicular to the tilt direction we calculate, suggesting that these results are in agreement. We also make some additional general comparisons; our observations of dipping interfaces/crustal anisotropy beneath stations RED and NCT, both located on the arc, are supported by the observations Schulte-Pelkum et al. (2020). Although we lack the station density to resolve the circular arrangements of layer strikes around the centers of the volcanoes, which they attribute to the dipping fabrics of magmatic rocks, we still see some strongly dipping/anisotropic interfaces in the crust beneath RED and NCT, likely recording similar features. Many of the features we observe exhibit combinations of two- and four-lobed signals (Figs. 7, 8, 13), suggesting that these interfaces are likely both dipping and anisotropic.

There is also evidence for anisotropy in the mantle wedge beneath both RED and NCT. Both stations suggest the presence of a low-velocity region whose top interface is located at ~60 km depth beneath the arc. On either side of this interface beneath NCT, there are two dipping and/or anisotropic features, both with approximately east-west tilt directions. Although no tilt direction was calculated for the ~70 km sin(θ) pulse beneath RED, the strength of the signal on the sin(θ) component may also be consistent with the presence of east- or west-dipping anisotropy at depth, which could indicate continuity of a mantle wedge structure beneath RED and NCT. Given the location directly beneath the arc, it is possible that this low-velocity zone and potential associated anisotropy reflect a zone of partial melting, with melt aligned via an SPO mechanism as a result of deformation; deformation may also lead to fast or slow axis alignments as has been discussed for other interfaces. Alternatively, this feature could be continuous with the velocity decreases we infer beneath CNP and HOM, although this seems less likely given that the forearc and sub-arc mantle wedge may not experience the same flow patterns (e.g., Kneller et al., 2008). A final possibility is that this represents a dipping feature within the mantle wedge and is not associated with anisotropy. Energy on the transverse component at a delay time of 0 s relative to the direct P arrival is indicative of a dipping interface at depth (Fig. 7a; e.g., Schulte-Pelkum and Mahan, 2014b; Olugboji and Park, 2016), increasing the likelihood of this last possible interpretation, but it is important to note that this is not conclusive given the evidence for complex, multilayered structure beneath this station in both the crust and mantle.

At depths below ~75 km, there are broad similarities in inferred geometries among the interfaces beneath RED and NCT, characterized by energy on the cos(2θ) component, indicating anisotropy oriented approximately N-S or *E*-W, depending on whether these interfaces are associated with the tops or bottoms of anisotropic layers, and whether they are the result of the alignment of fast or slow symmetry axes. Beneath NCT, a pair of pulses above and below the ~80 km velocity decrease could represent the top and bottom of an anisotropic layer. If this is the case, and if it is assumed that in the mantle this anisotropy is more likely associated with fast axis alignment of olivine, this would suggest anisotropy oriented approximately N-S. This could reflect the presence of sheared A-, C-, or E-type olivine within the mantle wedge (Karato et al., 2008; Long, 2013). The contrast between this anisotropic orientation and the east or west orientation of the low-velocity layer at ~60 km discussed above indicates that anisotropic orientation in the mantle wedge changes with depth. This could be the result of oblique subduction and/or the adjacent flat slab leading to different flow directions and thus different orientations of anisotropy at different depths within the mantle wedge (e.g., Kneller and van Keken, 2008), or the result of an arc-related process such as SPO of partial melt, as discussed above. If the shallower pair of sin(θ) pulses is interpreted as the top and bottom of an anisotropic layer with a fast symmetry axis, this suggests east-dipping anisotropy. The model of Kneller and van Keken (2008) would predict anisotropy dipping in the direction of increasing slab dip (here approximately west), perhaps making the melt SPO interpretation more likely. In either case, these results suggest a change in anisotropic orientation with depth beneath the arc.

We can make some general comparisons between our mantle wedge observations and anisotropy results obtained with other techniques, including anisotropic tomography (Tian and Zhao, 2012; Wang and Tape, 2014; Gou et al., 2019) and shear wave splitting (Hanna and Long, 2012; Perttu et al., 2014; Venereau et al., 2019; McPherson et al., 2020; Karlowska et al., 2021; Richards et al., 2021). The change in fast axis orientation with depth beneath NCT discussed above can also be observed beneath Mt. Redoubt (close to our stations RED and NCT) in the anisotropic body wave tomography results of Tian and Zhao (2012), and slightly further southwest in the results of Gou et al. (2019). The anisotropic surface wave tomography results of Wang and Tape (2014) indicate that for a period of 40s (which they suggest best characterizes anisotropy between 40 and 120 km depth), anisotropy is primarily oriented NW-SE across the region covered by our Kenai transect, approximately parallel to Pacific plate motion. While we do observe interfaces with these orientations throughout our Kenai transect, our results suggest significantly more complex anisotropy in this region.

For stations on the western end of the Kenai Peninsula, the area imaged by the Kenai transect in this study, the SKS splitting measurements of Hanna and Long (2012), Perttu et al. (2014), Venereau et al. (2019), and McPherson et al. (2020) suggest that fast splitting directions are subduction-parallel in the forearc; furthermore, Venereau et al. (2019) and McPherson et al. (2020) document a transition to trench-parallel beneath the arc. McPherson et al. (2020) attribute this shift to a change in the anisotropic volumes sampled by the teleseismic SKS phases; in the forearc, the mantle wedge is thin so the splitting signal probably comes primarily from the slab, but in the backarc where the mantle wedge is thicker, the SKS phases instead reflect more of the wedge anisotropy signal. Conversely, the local S wave splitting results of Karlowska et al. (2021) and Richards et al. (2021) suggest a transition from arc-parallel fast directions in the forearc to approximately arc-perpendicular fast directions in the backarc. Richards et al. (2021) also show that fast directions are approximately NW-SE beneath the Kenai Peninsula, where the forearc stations closest to the trench are located. Station NCT, for which we infer anisotropic fast directions in the mantle wedge, is located near the arc and also near the transition from arc-parallel fast directions to arc-perpendicular fast directions (oriented approximately east-west, as the arc is oblique to the trench and is closer to N-S in this part of the subduction zone; see Fig. 1) documented by Richards et al. (2021). As discussed above, the inferred fast directions beneath NCT appear to change with depth, with approximately *E*-W oriented anisotropy at ~60 km and approximately N-S oriented anisotropy at ~80 km. The shallower low-velocity region with anisotropy oriented approximately E-W is in agreement with the fast splitting directions of Richards et al. (2021), perhaps indicating that this layer exerts a stronger control on their observed fast direction. Richards et al. (2021) also suggest that beneath the Kenai Peninsula, where the mantle wedge is thin, fast directions are oriented approximately subduction-parallel, and that this signal originates in the slab. This could be consistent with the anisotropy we observe at or near the slab top beneath CNP and HOM, although the fast directions we infer within the slab are somewhat variable and are not oriented consistently NW-SE, again revealing complexity at depth that is not discernable via the path-integrated measurements obtained from shear wave splitting.

Karlowska et al. (2021) suggested that trench-parallel fast directions they observe in the forearc via local shear wave splitting are potentially related to mantle wedge serpentinization near the slab top. As discussed above, it is possible that there is a continuous layer of serpentinite at the slab surface between CNP and HOM, if we assume that these interfaces are associated with slow axis alignment and the top of the anisotropic layer. A layer of serpentinite at or above the plate interface has also been documented in the forearc regions of other subduction zones (e.g., Bostock et al., 2002; Schulte-Pelkum and Mahan, 2014a; Nikulin et al., 2009; McCormack et al., 2013; Wagner et al., 2013). However, it has also been suggested that the mantle wedge here may be too dry to lead to significant serpentinization (e.g., Abers et al., 2017). Alternatively, if the interfaces we observe are instead a result of fast axis alignment, this would indicate a NW-SE orientation of anisotropy beneath CNP and a subduction-parallel dip direction beneath HOM, and would thus argue against serpentinite as the source of the anisotropic signal. In this case, our results could potentially suggest shearing along the slab-mantle interface. Our results may also indicate the likely presence of another layer of anisotropy in the shallower mantle wedge beneath HOM and possibly CNP (depending on the inferred Moho depth; see section 3.1.1), which we suggest could be attributed to mantle wedge deformation, although the complexity of the two- and four-lobed terms makes it difficult to identify a fast direction and therefore a specific feature or fabric, as discussed above.

4.2.2. *Yakutat transect*

Fig. 14 indicates that there is significant deformation in the crust of the overlying plate beneath the Yakutat transect, likely the result of subduction of the overthickened Yakutat slab (e.g., Plafker and Berg, 1994; Eberhart-Phillips et al., 2006). Several large-scale features become apparent when looking at this transect collectively. First, tilt directions within the continental crust appear to be generally consistent for HIN and PWL, although SAW exhibits some variability. Beneath HIN, the $k = 1$ features identified show primarily NW-SE orientations, while orientations are primarily ENE-WSW beneath PWL. Distribution of energy on the $k = 2$ terms is also relatively consistent beneath HIN and PWL as well as SAW, primarily on the $\sin(2\theta)$ term for HIN and PWL, and the $\cos(2\theta)$ term for SAW. Additionally, the primary orientation of crustal features appears to change moving away from the trench along the transect. Beneath HIN, $k = 1$ features are approximately subduction-parallel, beneath PWL, $k = 1$ features are approximately NE-SW, and beneath SAW, $k = 1$ features transition from a NW-SE orientation at the shallower ~20 km interface to near E-W at ~30 km.

Beneath PWL and SAW, additional interpretations can be made for the $k = 2$ terms in the crust. If the pair of $\sin(2\theta)$ pulses on either side of the ~15 km interface beneath PWL represent the top and bottom of anisotropic layer, and if it is assumed that slow axis alignment is more common among crustal minerals (e.g., Brownlee et al., 2017), this suggests anisotropy aligned NW-SE, in contrast with the NE-SW tilt directions beneath PWL. Beneath SAW, a similar analysis can be done for the pair of $\cos(2\theta)$ pulses surrounding the ~20 km interface, which suggests an approximately east-west orientation. This would be more consistent with the deeper ~30 km tilt direction. Crustal deformation appears to be taking place along the entire length of the transect, but our observations suggest that the geometry of deformation is complex and changes with increasing distance from the trench.

Similar to our inferences beneath the Kenai transect, the results of Schulte-Pelkum et al. (2020) also indicate strong anisotropic/dipping signals in the crust in the Yakutat transect region, consistent with our results. In general, we observe tilt directions approximately perpendicular to the strikes they obtain at similar depths beneath our Yakutat stations, with the exception of SAW, where they determine a strike for a crustal interface shallower than the interfaces we interpret. However, we do observe a strong $\cos(\theta)$ pulse at short delay times on the SAW harmonic decomposition gather (Fig. 11b), which would be consistent with the approximately east-west strike that they obtain for their identified layer beneath SAW. The relative consistency in tilt direction with depth beneath HIN and PWL would seem to support the general observation of Schulte-Pelkum et al. (2020) that orientation of dipping/anisotropic fabrics does not change significantly with depth in Alaska, although they note that above the Yakutat slab, the strikes of deep crustal interfaces may parallel the depth contours of the Yakutat slab more closely than shallower interfaces.

At the three stations for which tilt directions were calculated at or very close to the overriding plate Moho – PWL, SAW, and GHO – the tilt directions appear to be generally similar along the profile (Fig. 14), close to E-W. This is perhaps indicative of an aspect of continental Moho structure that is continuous along the length of the transect. Such a feature could be related to shearing either just above or just below the overriding plate Moho, in the lowermost crust or uppermost mantle, likely as a result of deformation associated with flat slab subduction. This signal could reflect the presence of deformed lower-crustal rocks, which seems likely because the interface at which this signal originates appears to be slightly above the Moho beneath station SAW. Another possible explanation is the presence of sheared olivine between the top of the flat slab and the overriding plate Moho. Identifying the specific olivine fabric present is not straightforward; while the interfaces beneath PWL and SAW could be interpreted as having fast axes normal to the subduction direction and therefore as indicative of B-olivine, the interface beneath GHO is somewhat closer to subduction-parallel, which would not be consistent with B-olivine. If sheared B-olivine is indeed the source of this signal, there are several potential explanations for the GHO interface: first, it is possible that this feature is only continuous beneath PWL and SAW, and not GHO; second, that the tilt direction calculated for the $\sin(\theta)$ pulse associated with this interface beneath GHO is influenced by the shoulder of the $\cos(\theta)$ pulse immediately beneath it (section 3.2.4; Fig. 12b); and third, that our inferred Moho interface beneath GHO is incorrect, and the true Moho is located deeper but does not appear as a prominent arrival on our RF gathers; the anisotropic interface at ~30 km, a depth similar to the Moho depths beneath PWL and SAW, could represent the continuation of this feature beneath GHO, with the true Moho also located around this depth. Another possible origin for this signal is the thin, low velocity layer identified between the slab crust and the overriding plate by Kim et al. (2014) and Mann et al. (2022), who suggest that this could be a layer of metasediments. Metasediments could also produce an anisotropic signal above the slab at shallow depths (Miller et al., 2018), but we do not observe a strong drop in velocity that would be consistent with a slow sedimentary layer (Kim et al., 2014; Miller et al., 2018; Mann et al., 2022). We do, however, observe a velocity decrease associated with anisotropy at ~40 km beneath SAW, which may correspond to the slab top. It is possible that this interface is associated with a low-velocity layer as observed by Kim et al. (2014) and Mann et al. (2022), and, if its origin is the same as that of the anisotropic layer beneath PWL, this could be indicative of a continuous sedimentary layer atop the Yakutat slab. However, this interface is ~10 km deeper than the depths inferred by Mann et al. (2022) for the top of the low-velocity layer in this region, so it is possible that it represents a different feature, or that we have obtained different depth estimates for the same feature.

Alternatively, if it is assumed that the negative velocity gradient at ~40 km beneath SAW represents the top of the slab and that anisotropy is due to fast axis alignment, this suggests a NE-SW orientation, which could be consistent with the presence of B-olivine and would suggest relatively cool and water-rich conditions near the slab top (Jung and Karato, 2001). Alternatively, serpentine slow axes would likely be aligned almost vertically for a very shallowly dipping slab (Katayama et al., 2009), assuming that the shear plane is still parallel to the subducting plate, which would be challenging to observe via receiver functions. However, Nikulin et al. (2019) have suggested that anisotropy that is not aligned with the subduction direction in flat slab settings may still be indicative of serpentinization if the serpentine slow axis orientation is locally controlled. Given the complexity of this flat slab setting, it is possible that the deformation leading to serpentine alignment may not be parallel to subduction. Additionally, an isotropic velocity decrease is observed at the same delay time as the $\sin(2\theta)$ pulse, which may also be indicative of serpentinite.

Serpentinization above the Yakutat slab would be consistent with previous studies using a variety of methods. Blakely et al. (2005) used gravity and magnetic anomalies to argue for the presence of a serpentinite in this region, and Rossi et al. (2006) also suggest that the mantle wedge could be serpentinized based on Vp/Vs ratios obtained from radial component RFs. It is important to note that the study area of Rossi et al. (2006) (the BEAAR array) is located north of SAW, but it is possible that this feature is continuous between the two transects, and we may be observing very early stages of dehydration in the subducting Yakutat slab beneath SAW. This could also be consistent with the results of Chuang et al. (2017), who attribute a high spatial concentration of tremors north of our study area to significant dehydration of the Yakutat slab. Although the slab contours they use suggest depths that are somewhat shallower than what we observe, the spatial relationship between the onset of dehydration beneath SAW and more intense dehydration to the north would be consistent, regardless of the exact depth at which dehydration is occurring. The seismic attenuation study of Stachnik et al. (2004), also using data from the BEAAR array, attributes high attenuation in the mantle wedge beneath the trenchward stations of that transect to dehydration of the Yakutat slab. If the shear direction is subduction-parallel, this would seem to make B-olivine the more likely interpretation, but more complex deformation may still be associated with serpentinization. Whether the signal we observe arises from B- type olivine or serpentine, however, there is evidence for a water-rich environment above the Yakutat slab. Hiett et al. (2022) suggest based on geochemical evidence that fluids released from the Peruvian flat slab mobilize additional volatiles in the overlying mantle and crust, and that these volatiles ultimately reach the surface; this indicates that the subduction and devolatilization of flat slabs, such as that beneath the Yakutat transect, may still make important contributions to global volatile cycling, even in the absence of a volcanic arc.

Due to the comparatively shallow inferred overriding plate Moho beneath GHO, we do observe interfaces within the mantle "wedge" at this station (Fig. 14). The two shallowest interfaces are located at depths similar to the mid to lower crust at the other stations in the transect, and appear to reflect a deformation pattern relatively similar to the continental crust at SAW: NW-SE tilt directions at shallower depths and cos (2θ)terms indicating N-S or E-W oriented anisotropy. Additionally, the tilt direction calculated ~30 km beneath GHO is similar in orientation to that calculated just above the Moho at SAW, also ~30 km deep. This similarity may indicate that the Moho at GHO is in fact deeper than our preferred interpretation suggests and is not a prominent feature on our RF gathers. The velocity increase at ~45 km is difficult to explain in this context. As discussed in section 3.2.4, we find it more likely that the slab top is associated with the dipping/anisotropic interface at ~50 km than the velocity decrease at ~55 km. The tilt direction for the ~50 km interface is approximately subduction-parallel, and the slab dip begins to steepen somewhat here, so it is very plausible this interface could be associated with the dipping slab top. We do not, however, observe the signal we attribute to serpentinization beneath SAW, which could suggest heterogeneity of the slab-mantle interface.

Interestingly, and perhaps surprisingly, there also appears to be some anisotropic layering within the slab itself (Fig. 14) along the Yakutat transect. Beneath PWL, there are at least two interfaces exhibiting anisotropy within the mantle lithosphere. These interfaces directly follow each other on the $\cos(2\theta)$ term, and thus may be associated with the top and bottom of an anisotropic layer. If these are related to fast axis alignment, this would suggest an east-west orientation for anisotropy. Within the slab mantle lithosphere beneath SAW, there appears to be significant anisotropy indicated by the $\cos(2\theta)$ term, beginning with a velocity decrease at ~70 km and extending down to ~100 km. Given that both PWL and SAW have $\cos(2\theta)$ energy originating in the slab mantle lithosphere, it is possible that these consistent signals could be associated with E-W oriented anisotropy characterizing the slab as a whole. This is inconsistent with SKS splitting and tomography studies in the Yakutat region, which both indicate trench-normal intra-slab fast velocity directions (Hanna and Long, 2012; McPherson et al., 2020; Tian and Zhao, 2012; Wang and Tape, 2014; Gou et al., 2019).

If there is indeed consistent E-W anisotropy in the slab mantle lithosphere and it is a result of fossil spreading, this also contradicts the inference of Venereau et al. (2019), who suggest N-S oriented fossil anisotropy for the Yakutat slab based on SKS splitting, although the extent to which fast directions inferred from SKS splitting are representative of the slab mantle lithosphere versus the sub-slab mantle is unclear. Hanna and Long (2012) suggest that their measurements are likely to be more representative of sub-slab mantle anisotropy than intra-slab anisotropy. Thus, it is possible that the SKS splitting studies are sampling the sub-slab mantle more strongly than the slab mantle lithosphere, and/or that the anisotropic layer we observe beneath PWL is not representative of anisotropy within the Yakutat slab mantle lithosphere in general, which is a strong possibility. Alternatively, it is also possible that the assumptions on which our inferred fast direction is based (i.e. aligned fast axes, and that the two interfaces beneath PWL represent the top and bottom of an anisotropic layer) are incorrect, or that this layer beneath a single station is not representative of the anisotropy within the rest of the slab. If the $k = 2$ signals in the slab are primarily associated with N-S anisotropy instead of E-W, this would be consistent with the inference of Venereau et al. (2019).

5. Conclusions

We have carried out a P-to-S receiver function study for south-central Alaska that characterizes the anisotropic structures of the crust, mantle wedge, and slab of both normally-dipping and flat slab segments of the Alaska subduction zone (Fig. 15). The isotropic structures we observe for both segments are in broad agreement with previous work, including other receiver function studies, shear wave splitting, and tomography. A detailed analysis of the anisotropic structure imaged by our receiver functions reveals significant differences between the two segments, as is likely to be expected for such contrasting subduction geometries. Beneath the Kenai transect, our results indicate the presence of dipping and anisotropic interfaces in the crust. Beneath the continental Moho, we observe serpentinization and/or shearing above the slab in the forearc mantle wedge and the development of contrasting anisotropic orientations with depth beneath the arc, possibly a result of oblique subduction and/or the adjacent neighboring flat slab, or melt SPO beneath the arc. There is evidence for overriding plate deformation in the forearc region above the Yakutat slab that broadly changes character along the transect as a result of deformation, and the orientations of the anisotropic/dipping interfaces are generally in agreement with previous work on crustal anisotropy in this region. There is also evidence for water-rich conditions in the Yakutat mantle wedge, consistent with previous studies using a variety of methods, and providing additional evidence for volatile cycling in flat slab settings. Our results provide additional constraints on subduction-related anisotropy in the crust, mantle wedge, and Pacific and Yakutat slabs beneath south-central Alaska, a highly tectonically active and complex region.

CRediT authorship contribution statement

Anne A. Haws: Writing – review & editing, Writing – original draft, Visualization, Methodology, Investigation, Formal analysis, Conceptualization. **Maureen D. Long:** Writing – review & editing, Supervision, Methodology, Conceptualization. **Yantao Luo:** Writing – review & editing, Visualization, Methodology.

Declaration of Competing Interest

The authors declare that they have no known competing financial interests or personal relationships that could have appeared to influence the work reported in this paper.

Data availability

All data are publically available via the IRIS (Incorporated Research Institutions for Seismology) Data Management Center (DMC).

Acknowledgements

We thank N. Bar, W.D. Frazer, and J. Park for assistance with RF calculation setup, and W.D. Frazer, J. Park, J. Wolf, and F. Link for helpful discussions. We used data from the Alaska Regional (AK; DOI: https://doi.org/10.7914/SN/AK) and the Alaska Volcano Observatory (AV; https://doi.org/10.7914/SN/AV) networks in this study. All data are publicly available via the Data Management Center (DMC) of the Incorporated Research Institutions for Seismology (IRIS) at https://ds.iris.edu/ds/nodes/dmc/. The facilities of the IRIS Consortium are supported by the National Science Foundation's Seismological Facilities for the Advancement of Geoscience (SAGE) Award under Cooperative Support Agreement EAR-1851048. This work was supported by Yale University. We are grateful for comments from anonymous reviewers that helped us to substantially improve the paper.

Appendix A. Supplementary data

Supplementary data to this article can be found online at https://doi.org/10.1016/j.tecto.2023.230112.

References

Abers, G.A., van Keken, P.E., Hacker, B.R., 2017. The cold and relatively dry nature of mantle forearcs in subduction zones. Nat. Geosci. 10, 333–337.
Bar, N., Long, M.D., Wagner, L.S., Beck, S.L., Zandt, G., Tavera, H., 2019. Receiver function analysis reveals layered anisotropy in the crust and upper mantle beneath southern Peru and northern Bolivia. Tectonophysics 753, 93–110.
Bezacier, L., Reynard, B., Bass, J.D., Sanchez-Valle, C., Van de Moortèle, B., 2010. Elasticity of antigorite, seismic detection of serpentinites, and anisotropy in subduction zones. Earth Planet. Sci. Lett. 289, 198–208.
Bianchi, I., Park, J., Piana Agostinetti, N., Levin, V., 2010. Mapping seismic anisotropy using harmonic decomposition of receiver functions: an application to Northern Apennines, Italy. J. Geophys. Res. 115, B12317.
Bishop, B.T., Beck, S.L., Zandt, G., Wagner, L., Long, M., Antonijevic, S.K., Kumar, A., Tavera, H., 2017. Causes and consequences of flat-slab subduction in southern Peru. Geosphere 13, 1392–1407.
Blakely, R.J., Brocher, T.M., Wells, R.E., 2005. Subduction-zone magnetic anomalies and implications for hydrated forearc mantle. Geology 33, 445–448.
Bostock, M.G., Hyndman, R.D., Rondenay, S., Peacock, S.M., 2002. An inverted continental Moho and serpentinization of the forearc mantle. Nature 417, 536–538.
Brownlee, S.J., Schulte-Pelkum, V., Raju, A., Mahan, K., Condit, C., Orlandini, O.F., 2017. Characteristics of deep crustal seismic anisotropy from a compilation of rock elasticity tensors and their expression in receiver functions. Tectonics 36, 1835–1857.
Christeson, G.L., Gulick, S.P.S., van Avendonk, H.J.A., Worthington, L.L., Reece, R.S., Pavlis, T.L., 2010. The Yakutat terrane: Dramatic change in crustal thickness across the transition fault, Alaska. Geology 38, 895–898.
Chuang, L., Bostock, M., Wech, A., Plourde, A., 2017. Plateau subduction, intraslab seismicity, and the Denali (Alaska) volcanic gap. Geology 45, 647–650.
Daly, K.A., Abers, G.A., Mann, M.E., Roecker, S., Christensen, D.H., 2021. Subduction of an oceanic plateau across Southcentral Alaska: High-Resolution Seismicity. J. Geophys. Res. Solid Earth 126 e2021JB022809.
Eakin, C.M., Long, M.D., Beck, S.L., Wagner, L.S., Tavera, H., Condori, C., 2014. Response of the mantle to flat slab evolution: Insights from local *S* splitting beneath Peru. Geophys. Res. Lett. 41, 3438–3446.
Eberhart-Phillips, D., Christensen, D.H., Brocher, T.M., Hansen, R., Ruppert, N.A., Haeussler, P.J., Abers, G.A., 2006. Imaging the transition from Aleutian subduction to Yakutat collision in Central Alaska, with local earthquakes and active source data. J. Geophys. Res. 111, B11303.
Ferris, A., Abers, G.A., Christensen, D.H., Veenstra, E., 2003. High resolution image of the subducted Pacific (?) plate beneath Central Alaska, 50-150 km depth. Earth Planet. Sci. Lett. 214, 575–588.
Ford, H.A., Long, M.D., Wirth, E.A., 2016. Midlithospheric discontinuities and complex anisotropic layering in the mantle lithosphere beneath the Wyoming and Superior Provinces. J. Geophys. Res. Solid Earth 121, 6675–6697.
Fuis, G.S., Moore, T.E., Plafker, G., Brocher, T.M., Fisher, M.A., Mooney, W.D., Nokleberg, W.J., Page, R.A., Beaudoin, B.C., Christensen, N.I., Levander, A.R., Lutter, W.J., Saltus, R.W., Ruppert, N.A., 2008. Trans-Alaska Crustal Transect and continental evolution involving subduction underplating and synchronous foreland thrusting. Geology 36, 267–270.
Gama, I., Fischer, K.M., Eilon, Z., Krueger, H.E., Dalton, C.A., Flesch, L.M., 2021. Shear-wave velocity structure beneath Alaska from a Bayesian joint inversion of Sp receiver functions and Rayleigh wave phase velocities. Earth Planet. Sci. Lett. 560, 116785.
Gama, I., Fischer, K.M., Hua, J., 2022. Maping the Lithosphere and Asthenosphere beneath Alaska with Sp Converted Waves. Geochem. Geophys. Geosyst. 23 e2022GC010517.
Gilbert, H., Beck, S., Zandt, G., 2006. Lithospheric and upper mantle structure of Central Chile and Argentina. Geophys. J. Int. 165, 383–398.
Gou, T., Zhao, D., Huang, Z., Wang, L., 2019. Aseismic Deep Slap and Mantle Flow beneath Alaska: Insight from Anisotropic Tomography. J. Geophys. Res. Solid Earth 124, 1700–1724.
Hanna, J., Long, M.D., 2012. SKS splitting beneath Alaska: Regional variability and implications for subductin processes at the slab edge. Tectonophysics 530-531, 272–285.
Hayes, G.P., Moore, G.L., Portner, D.E., Hearne, M., Flamme, H., Furtney, M., Smoczyk, G.M., 2018. Slab2, a comprehensive subduction zone geometry model. Science 362, 58–61.
Hiett, C.D., Newell, D.L., Jessup, M.J., Grambling, T.A., Scott, B.E., Upin, H.E., 2022. Deep CO_2 and N_2 emissions from Peruvian hot springs: Stable isotopic constraints on volatile cycling in a flat-slab subduction zone. Chem. Geol. 595, 120797.
Horn, C., Bouilhol, P., Skemer, P., 2020. Serpentinization, Deformation, and Seismic Anisotropy in the Subduction Mantle Wedge (2020). Geochem. Geophys. Geosyst. 21 e2020GC008950.
Jung, H., 2011. Seismic anisotropy produced by serpentine in mantle wedge. Earth Planet. Sci. Lett. 307, 535–543.
Jung, H., Karato, S., 2001. Water-induced fabric transitions in olivine. Science 293, 1460–1463.
Karato, S., Jung, H., Katayama, I., Skemer, S., 2008. Geodynamic significance of Seismic Anisotropy of the Upper Mantle: New Insights from Laboratory Studies. Annu. Rev. Earth Planet. Sci. 36, 59–95.
Karlowska, E., Bastow, I.D., Rondenay, S., Martin-Short, R., Allen, R.M., 2021. The development of seismic anisotropy below south-Central Alaska: evidence from local earthquake shear wave splitting. Geophys. J. Int. 225, 548–554.
Katayama, I., Hirauchi, K., Michibayashi, K., Ando, J., 2009. Trench-parallel anisotropy produced by serpentine deformation in the hydrated mantle wedge. Nature 461, 1114–1117.
Kennett, B.L.N., Engdahl, E.R., Buland, R., 1995. Constraints on seismic velocities in the Earth from traveltimes. Geophys. J. Int. 122, 108–124.
Kneller, E.A., van Keken, P.E., 2008. Effect of three-dimensional slab geometry on deformation in the mantle wedge: Implications for shear wave anisotropy. Geochem. Geophys. Geosyst. 9, Q01003.
Kneller, E.A., van Keken, P.E., Karato, S., Park, J., 2005. B-type olivine fabric in the mantle wedge: Insights from high-resolution non-Newtonian subduction zone models. Earth Planet. Sci. Lett. 237, 781–797.
Kim, Y., Abers, G.A., Li, J., Christensen, D., Calkins, J., Rondenay, S., 2014. Alaska Megathrust 2: Imaging the megathrust zone and Yakutat/Pacific plate interface in the Alaska subduction zone. J. Geophys. Res. Solid Earth 119, 1924–1941.
Kneller, E.A., Long, M.D., van Keken, P.E., 2008. Olivine fabric transitions and shear wave anisotropy in the Ryukyu subduction system. Earth Planet. Sci. Lett. 268, 268–282.
Krueger, H.E., Wirth, E.A., 2017. Investigating Segmentation in Cascadia: Anisotropic Crustal Structure and Mantle Wedge Serpentinization from Receiver Functions. Geochem. Geophys. Geosyst. 18, 3592–3607.
Kumar, A., Wagner, L.S., Beck, S.L., Long, M.D., Zandt, G., Young, B., Tavera, H., Minaya, E., 2016. Seismicity and state of stress in the central and southern Peruvian flat slab. Earth Planet. Sci. Lett. 441, 71–80.
Levin, V., Park, J., 1997. *P-SH* conversions in a flat-layered medium with anisotropy of arbitrary orientation. Geophys. J. Int. 131, 253–266.
Li, J., Abers, G.A., Kim, Y., Christensen, D., 2013. Alaska megathrust 1: Seismicity 43 years after the great 1964 Alaska megathrust earthquake. J. Geophys. Res. Solid Earth 118, 4861–4871.
Long, M.D., 2013. Constraints on subduction geodynamics from seismic anisotropy. Rev. Geophys. 51, 76–112.
Mainprice, D., Ildefonse, B., 2009. Seismic Anisotropy of Subduction Zone Minerals-Contribution of Hydrous Phases. In: Lallemand, S., Funiciello, F. (Eds.), Subduction Zone Geodynamics, pp. 63–84.
Mann, M.E., Abers, G.A., Daly, K.A., Christensen, D.H., 2022. Subduction of an Oceanic Plateau across Southcentral Alaska: Scattered-Wave Imaging. J. Geophys. Res. Solid Earth 127 e2021JB022697.
Martin-Short, R., Allen, R.M., Bastow, I.D., 2016. Subduction geometry beneath south Central Alaska and its relationship to volcanism. Geophys. Res. Lett. 43, 9509–9517.
Martin-Short, R., Allen, R., Bastow, I.D., Porritt, R.W., Miller, M.S., 2018. Seismic Imaging of the Alaska Subduction Zone: Implications for Slab Geometry and Volcanism. Geochem. Geophys. Geosyst. 19, 4541–4560.
McCormack, K., Wirth, E.A., Long, M.D., 2013. B-type olivine fabric and mantle wedge serpentinization beneath the Ryukyu arc. Geophy. Res. Lett. 40, 1697–1702.
McPherson, A.M., Christensen, D.H., Abers, G.A., Tape, C., 2020. Shear Wave Splitting and Mantle Flow beneath Alaska. J. Geophys. Res. Solid Earth 123 e2019JB018329.
Miller, M.S., O'Driscoll, L.J., Porritt, R.W., Roeske, S.M., 2018. Multiscale crustal architecture of Alaska inferred from P receiver functions. Lithosphere 10, 267–278.
Nikulin, A., Levin, V., Park, J., 2009. Receiver function study of the Cascadia megathrust: evidence for localized serpentinization. Geochem. Geophys. Geosyst. 10, Q07004.
Nikulin, A., Levin, V., Carr, M., Herzberg, C., West, M., 2012. Evidence for two upper mantle sources driving volcanism in Central Kamchatka. Earth Planet. Sci. Lett. 321-322, 14–19.
Nikulin, A., Bourke, J.R., Domino, J.R., Park, J., 2019. Tracing Geophysical Indicators of Fluid-Induced Serpentinization in the Pampean Flat Slab of Central Chile. Geochem. Geophys. Geosyst. 20 https://doi.org/10.1029/2019GC008491.
Olugboji, T.M., Park, J., 2016. Crustal anisotropy beneath Pacific Ocean-Islands from harmonic decomposition of receiver functions. Geochem. Geophys. Geosyst. 17, 810–832.
Park, J., Levin, V., 2000. Receiver Functions from Multiple-Taper Spectral Correlation estimates. Bull. Seismol. Soc. Am. 90, 1507–1520.

Park, J., Levin, V., 2016. Anisotropic shear zones revealed by backazimuthal harmonics of teleseismic receiver functions. Geophys. J. Int. 207, 1216–1243.
Park, J., Yuan, H., Levin, V., 2004. Subduction zone anisotropy beneath Corvallis, Oregon: a serpentinite skid mark of trench-parallel terrane migration? J. Geophys. Res. 109, B10306.
Perttu, A., Christensen, D., Abers, G., Song, X., 2014. Insights into mantle structure and flow beneath Alaska based on a decade of observations of shear wave splitting. J. Geophys. Res. Solid Earth 119, 8366–8377.
Plafker, G., Berg, H.C., 1994. Overview of the geology and tectonic evolution of Alaska. In: Plafker, G., Berg, H.C. (Eds.), The Geology of Alaska. The Geology of North America G-1, pp. 989–1021.
Richards, C., Tape, C., Abers, G.A., Ross, Z.E., 2021. Anisotropy Variations in the Alaska Subduction Zone based on Shear-Wave Splitting from Intraslab Earthquakes. Geochem. Geophys. Geosyst. 22 e2020GC009558.
Rondenay, S., Abers, G.A., van Keken, P.E., 2008. Seismic imaging of subduction zone metamorphism. Geology 36, 275–278.
Rondenay, S., Montési, L.G.J., Abers, G.A., 2010. New geophysical insight into the origin of the Denali volcanic gap. Geophys. J. Int. 182, 613–630.
Rossi, G., Abers, G.A., Rondenay, S., Christensen, D.H., 2006. Unusual mantle Poisson's ratio, subduction, and crustal structure in Central Alaska. J. Geophys. Res. 111. B09311.
Schulte-Pelkum, V., Mahan, K.H., 2014a. A method for mapping crustal deformation and anisotropy with receiver functions and first results from USArray. Earth Planet. Sci. Lett. 402, 221–233.
Schulte-Pelkum, V., Mahan, K.H., 2014b. Imaging Faults and Shear zones using Receiver Functions. Pure Appl. Geophys. 171, 2967–2991.
Schulte-Pelkum, V., Caine, J.S., Jones III, J.V., Becker, T.W., 2020. Imaging the Tectonic grain of the Northen Cordillera Orogen using Transportable Array Receiver Functions. Siesmol. Res. Lett. 91, 3086–3105.
Stachnik, J.C., Abers, G.A., Christensen, D.H., 2004. Seismic attenuation and mantle wedge temperatures in the Alaska subduction zone. J. Geophys. Res. 109, B10304.
Tian, Y., Zhao, D., 2012. Seismic anisotropy and heterogeneity in the Alaska subduction zone. Geophys. J. Int. 190, 629–649.
Venereau, C.M.A., Martin-Short, R., Bastow, I.D., Allen, R.M., Kounoudis, R., 2019. The Role of Variable Slab dip in Driving Mantle Flow at the Eastern Edge of the Askan Subduction margin: Insights from Shear-Wave Splitting. Geochem. Geophys. Geosyst. 20, 2433–2448.
Wagner, L.S., Beck, S., Zandt, G., Ducea, M.N., 2006. Depleted lithosphere, cold, trapped asthenosphere, and frozen melt puddles above the flat slab in Central Chile and Argentina. Earth Planet. Sci. Lett. 245, 289–301.
Wagner, L.S., Fouch, M.J., James, D.E., Long, M.D., 2013. The role of hydrous phases in the formation of trench parallel anisotropy: evidence from Rayleigh waves in Cascadia. Geophys. Res. Lett. 40, 1–5.
Wang, Y., Tape, C., 2014. Seismic velocity structure and anisotropy of the Alaska subduction zone based on surface wave tomography. J. Geophys. Res. Solid Earth 119, 8845–8865.
Wirth, E.A., Long, M.D., 2012. Multiple layers of seismic anisotropy and a low-velocity region in the mantle wedge beneath Japan: evidence from teleseismic receiver functions. Geochem. Geophys. Geosyst. 13, Q08005.
Worthington, L.A., Van Avendonk, H.J.A., Gulick, S.P.S., Christeson, G.L., Pavlis, T.L., 2012. Crustal structure of the Yakutat terrane and the evolution of subduction and collision in southern Alaska. J. Geophys. Res. 117, B01102.
Zhang, Y., Li, A., Hu, H., 2019. Crustal Structure in Alaska from Receiver Function Analysis. Geophys. Res. Lett. 46, 1284–1292.
Zhao, D., Christensen, D., Pulpan, H., 1995. Tomographic imaging of the Alaska subduction zone. J. Geophys. Res. 100, 6487–6504.